



UNIVERSITY
OF TRENTO

DIPARTIMENTO DI INGEGNERIA E SCIENZA DELL'INFORMAZIONE

38123 Povo – Trento (Italy), Via Sommarive 14
<http://www.disi.unitn.it>

ADS-BASED ARRAY DESIGN FOR 2D AND 3D ULTRASOUND
IMAGING

G. Oliveri and A. Massa

January 2010

Technical Report # DISI-11-098

ADS-based Array Design for 2D and 3D Ultrasound Imaging

G. Oliveri and A. Massa

ELEDIA Research Group

Department of Information and Communication Technologies,

University of Trento, Via Sommarive 14, 38050 Trento - Italy

Tel. +39 0461 882057, Fax +39 0461 882093

E-mail: *andrea.massa@ing.unitn.it, giacomo.oliveri@dit.unitn.it*

Web-site: *http://www.eledia.ing.unitn.it*

ADS-based Array Design for 2D and 3D Ultrasound Imaging

G. Oliveri and A. Massa

Abstract

This paper describes a class of non-overlapping layouts based on Almost Difference Sets for ultrasound applications. Thanks to the mathematical properties of ADSs, such arrays provide good radiation properties with far-field peak sidelobe levels belonging to an *a-priori* predictable set of analytically-derived bounds. An extensive numerical analysis, including near-field simulations, is provided to assess the reliability and the features of the proposed design methodology for both linear and planar arrays.

Key words: Array Antennas, Interleaved Arrays, Almost Difference Sets, Sidelobe Control, Pulse-Echo Pattern, Two-Way Radiation Pattern.

1 Introduction

Real-time ultrasound imaging techniques have several applications in underwater and sonar systems, biomedical diagnostics, and non-invasive surgery [1][2][3][4][5][6][7]. In order to provide adequate resolution and contrast, real time two- and three-dimensional systems require 1D/2D transducer arrays with hundred or thousand elements [2]. Non-overlapping or interleaved layouts, where each element is used either in transmission or in reception, provide several advantages in terms of costs, weight, processing power, fabrication, and interconnection complexity [1][2]. However, interleaving transmitting and receiving arrays reduces the control of the peak sidelobe level (PSL) compared to the corresponding filled layouts. To overcome such a drawback, random approaches [8], semi-random approaches [1], and sparse periodic layouts (e.g., Vernier arrays) [3][9] have been proposed. Improved performances have been obtained by means of optimization methods, such as genetic algorithms [10], linear programming [11], and simulated annealing [5][12]. Despite their effectiveness in dealing with complex cost functions, optimization techniques usually require high computational costs and they are sometimes affected by convergence problems especially when dealing with large apertures. Moreover, it is often difficult to *a-priori* provide reliable predictions of the achievable radiation properties because of their intrinsic randomness.

In this paper, a new analytical methodology is proposed to design non-overlapping transducer layouts with good and predictable radiation properties. The objective of the paper is not to determine an optimal interleaving scheme for a specific problem, but rather (a) to provide simple and reliable design guidelines to be used when a computationally efficient and sub-optimal solution is preferred to a random or a stochastically-optimized array or/and (b) to give a better initialization for a successive global optimization aimed at determining the “optimal” solution. Towards this end, the array synthesis is faced with an innovative approach based on the so-called Almost Difference Sets (ADS s). ADS s are binary sequences characterized by a three-level autocorrelation [13]. They are a generalization of Difference Sets [14][15][16]. ADS properties have already been exploited to thin linear [17] and planar [18] arrays with controllable sidelobes. The design of non-overlapping transducer layouts based on ADS sequences is motivated by the following key-observations: (a) the complementary of an ADS is still an ADS [14]; (b) an

ADS-based array has a low and predictable *PSL* [17][18]; (c) *ADS* arrangements can be analytically designed without any optimization and whatever the aperture size [17]. Furthermore, non-overlapping *ADS* layouts can be synthesized by simply assigning the elements either to the transmitting or to the receiving array according to the sequence of 0s or 1s of an *ADS*. On the other hand, it should be also pointed out that the use of *ADS*s for such a purpose is not granted by a straightforward exploitation of the results obtained in [17][18]. Unlike thinned arrays, the performances of an imaging system are related to its *pulse-echo* (or *two-way*) radiation pattern [1][2]. Therefore, the bounds determined in [17][18] for *one-way* patterns of *ADS* arrangements do not apply. New theoretical and numerical analyses are then mandatory to deduce and validate suitable *a-priori* estimates for the performances of *ADS*-based arrangements for ultrasound imaging systems.

The outline of the paper is as follows. After a short review on array thinning through *ADS*s (Sect. 2), a theoretical analysis concerned with *ADS*-based non-overlapping layouts is provided. The key features of the arising two-way radiation patterns are then highlighted (Sect. 3). Section 4 describes some validation tests and numerical simulations of representative 1D and 2D *ADS* designs. Finally, some conclusions are drawn (Sect. 5).

2 ADS-Based Thinning

The *one-way* array factor of a planar arrangement defined over a lattice of $P \times Q$ positions ($N = P \times Q$ being the total number of elements) is equal to [19]

$$S_T(u, v) = \sum_{p=0}^{P-1} \sum_{q=0}^{Q-1} a_T(p, q) \exp[2\pi i (ps_x u + qs_y v)] \quad (1)$$

where $a_T(p, q)$ is the array weight of the (p, q) -th element, s_x and s_y are the lattice spacings along the x and y directions (in wavelengths), $u = \sin(\theta)\cos(\phi)$, $v = \sin(\theta)\sin(\phi)$ ($u^2 + v^2 \leq 1$)⁽¹⁾. Dealing with equally-weighted thinned arrays, $a_T(p, q)$, $p = 0, \dots, P - 1$, $q = 0, \dots, Q - 1$ can either assume the value 1 or 0 when an element is present or not at the (p, q) -th lattice position. In *ADS*-based thinning techniques [17][18], the lattice weights are selected as follows

⁽¹⁾ Linear arrays correspond to the case $Q = 1$.

$$a_T(p, q) = \begin{cases} 1 & \text{if } (p, q) \in \mathbf{A}_T \text{ [} p \in \mathbf{A}_T \text{ in the linear case]} \\ 0 & \text{otherwise} \end{cases} \quad (2)$$

where \mathbf{A}_T is a (N, K_T, Λ_T, t) -ADS (i.e., a K_T -subset of $\mathbf{G} \triangleq \mathbb{Z}^P \otimes \mathbb{Z}^Q$),⁽²⁾ N is the array size, K_T the number of active elements, and Λ_T and t are parameters which define the autocorrelation properties of the considered ADS (as discussed below). As a visual example, the $(18, 9, 4, 13)$ -ADS, i.e.

$$\mathbf{A}_T = \{0, 1, 5, 6, 7, 8, 10, 12, 15\}$$

(linear case [20]) is considered, and the associated $a_T(p)$ is provided in Fig. 1(a). By exploiting the properties of the autocorrelation function, $\xi_T(\tau_x, \tau_y) \triangleq \sum_{p=0}^{P-1} \sum_{q=0}^{Q-1} a_T(p, q) a_T[(p + \tau_x)|_{\text{mod } P}, (q + \tau_y)|_{\text{mod } Q}]$ ($P \times Q$ being its period), of ADS-binary sequences [13][14][15], which is known to be the following three-level function

$$\xi_T(\tau_x, \tau_y) = \begin{cases} K_T & (\tau_x, \tau_y) = 0 \\ \Lambda_T & \text{for } t \text{ values of } (\tau_x, \tau_y) \\ \Lambda_T + 1 & \text{otherwise,} \end{cases} \quad (3)$$

it turns out that [17][18] the power pattern $|S_T(u, v)|^2$ of an ADS-based array satisfies the following constraint

$$\left| S_T\left(\frac{k}{s_x P}, \frac{l}{s_y Q}\right) \right|^2 = \Xi_T(k, l) \quad k = 0, \dots, P-1, l = 0, \dots, Q-1 \quad (4)$$

i.e., the samples to the power pattern are equal to the inverse discrete Fourier transform (IDFT) of the autocorrelation function $\xi_T(\tau_x, \tau_y)$, $\Xi_T(k, l) \triangleq \sum_{\tau_x=0}^{P-1} \sum_{\tau_y=0}^{Q-1} \xi_T(\tau_x, \tau_y) \exp\left[2\pi i \left(\frac{\tau_x k}{P} + \frac{\tau_y l}{Q}\right)\right]$, which, from (3), turns out to be equal to

$$\Xi_T(k, l) = K_T - \Lambda_T + N\Lambda_T \delta(k, l) + \Psi(k, l). \quad (5)$$

In (5), $\delta(k, l)$ is the discrete impulse function [$\delta(k, l) = 1$ if $k = l = 0$ and $\delta(k, l) = 0$, otherwise], $\Psi(k, l) \triangleq \text{IDFT}\{\psi(\tau_x, \tau_y)\}$ being $\psi(t_x, t_y) \triangleq \sum_{r=1}^{N-1-t} \delta(\tau_x - \tau_x^r, \tau_y - \tau_y^r)$, and

⁽²⁾In this paper, a K_T -subset of \mathbf{G} indicates a set of K_T unique elements belonging to \mathbf{G} ; moreover $\mathbf{G} = \{(0, 0), (0, 1), \dots, (P-1, Q-1)\}$ if $Q > 1$, while $\mathbf{G} = \{0, 1, \dots, P-1\}$ if $Q = 1$.

(τ_x^r, τ_y^r) , $r = 1, \dots, N - 1 - t$, are the indexes at which $\xi_T(\tau_x^r, \tau_y^r) = \Lambda_T + 1$ [18] (an analogous relationship holds true in the linear case [17]). In order to clarify such properties, Figs. 1(b) and 1(c) provide an example of $\xi_T(\tau)$ and $S_T(u)$ for the arrangement represented in Fig. 1(a) (without loss of generality the linear case is taken into account). According to Eq. (3), the *ADS* sequence exhibits a three-level autocorrelation function [Fig. 1(b)], while the samples of the associated power pattern are confirmed to be equal to $\Xi_T(k)$ [Fig. 1(c)].

Thanks to (4), the following *a-priori* bounds have been derived for the *one-way PSLs* of *ADS*-based thinned arrays:

$$PSL_T^{INF} \leq PSL_T^{MIN} \leq PSL_T^{OPT} \leq PSL_T^{MAX} \leq PSL_T^{SUP}. \quad (6)$$

where $PSL_T^{OPT} \triangleq \min_{\sigma_x, \sigma_y} \left\{ PSL \left[\mathbf{A}_T^{(\sigma_x, \sigma_y)} \right] \right\}$, $\sigma_x = 0, \dots, P-1$, $\sigma_y = 0, \dots, Q-1$, $PSL \left[\mathbf{A}_T^{(\sigma_x, \sigma_y)} \right] \triangleq \frac{\max_{(u,v) \notin M_T} |S^{(\sigma_x, \sigma_y)}(u,v)|^2}{|S^{(\sigma_x, \sigma_y)}(u_0, v_0)|^2}$, (u_0, v_0) is the mainlobe steering direction, M_T is the mainlobe region defined as in [16], $|S^{(\sigma_x, \sigma_y)}(u, v)|^2$ is the power pattern of the layout generated from the cyclically-shifted version $\mathbf{A}_T^{(\sigma_x, \sigma_y)}$, $\mathbf{A}_T^{(\sigma_x, \sigma_y)} \triangleq \left\{ \left((p + \sigma_x)_{\text{mod } P}, (q + \sigma_y)_{\text{mod } Q} \right); (p, q) \in \mathbf{A}_T; \sigma_x, \sigma_y \in \mathbb{Z} \right\}$, of the reference *ADS*. The analytic expressions of the bounds in (6) are reported in the Appendix for both the linear case and the planar one. Equation (6) states that the peak sidelobe level of *ADS*-based arrays is constrained by the *a-priori* known quantities PSL_T^{INF} , PSL_T^{MIN} , PSL_T^{MAX} , and PSL_T^{SUP} .

Properties, construction techniques, and theorems concerned with *ADSs* can be found in [13][14][15], while explicit numerical expressions of linear and planar *ADS* sequences are available in [20].

3 ADS-based Non Overlapping Layouts - Mathematical Formulation

Let us consider the following theorem:

Theorem 1 [14] - If \mathbf{A}_T is an *ADS* then its complementary set $\mathbf{A}_R \triangleq \mathbf{G} \setminus \mathbf{A}_T$, (i.e., $\mathbf{A}_R = \{(p, q) \in \mathbf{G} : (p, q) \notin \mathbf{A}_T\}$) is an (N, K_R, Λ_R, t) -*ADS*, where $K_R = N - K_T$ and $\Lambda_R = N - 2K_T + \Lambda_T$.

Accordingly, starting from an *ADS* transmitting array with weights $a_T(p, q)$, $p = 0, \dots, P - 1$, $q = 0, \dots, Q - 1$, the coefficients of the receiving array $a_R(p, q)$ are simply obtained as $a_R(p, q) = 1 - a_T(p, q)$. The *ADS* layout is then composed by a rectangular aperture of $P \times Q$ transducers: K_T transducers for the transmission and the remaining $K_R = N - K_T$ for the reception. To provide an illustrative example, the arrangements coming from the (88, 44, 21, 22)-*ADS* (linear case [20]) and the (49, 25, 12, 24)-*ADS* (planar case [20]) are provided in Fig. 2. It is worth noticing that when $Q = 1$ (linear case), $N = P$ and $a_T(p, q) = a_T(p)$, $a_R(p, q) = a_R(p)$ [Fig. 2(a)].

Since each of the two non-overlapping arrays is an *ADS* arrangement, the following properties hold true: (a) both arrays are expected to exhibit low *one-way PSLs*; (b) each design can be cyclically shifted to obtain up to $P \times Q$ different layouts; (c) the computational costs to carry out a new array design is negligible (just a simple shift) for any aperture size. Moreover, it can be shown that the autocorrelation functions of the two arrays are equal except for an offset of $N(1 - 2\nu)$ ($\nu \triangleq \frac{K_T}{N}$)

$$\xi_R(\tau_x, \tau_y) = \xi_T(\tau_x, \tau_y) + N(1 - 2\nu). \quad (7)$$

Therefore, the corresponding *IDFTs* differ only in the origin of the $k - l$ plane

$$\Xi_R(k, l) = \Xi_T(k, l) + N^2(1 - 2\nu)\delta(k, l), \quad (8)$$

where $\Xi_R(k, l) \triangleq \sum_{\tau_x=0}^{P-1} \sum_{\tau_y=0}^{Q-1} \xi_R(\tau_x, \tau_y) \exp\left[2\pi i \left(\frac{\tau_x k}{P} + \frac{\tau_y l}{Q}\right)\right]$ and $\xi_R(\tau_x, \tau_y)$ are the unbalancing factor and the autocorrelation function of \mathbf{A}_R , respectively.

As regards the performances of *ADS* layouts for ultrasound imaging, it is worth to notice that the quality of ultrasound images is related to the two-way continuous wave (*CW*) radiation pattern defined in the far field as the product of the transmit and receive power pattern [1][3][9][2]

$$|S_{CW}(u, v)|^2 \triangleq |S_T(u, v)|^2 \times |S_R(u, v)|^2. \quad (9)$$

By using (4), (8), (9), (5) and through simple mathematical manipulations it results that the samples of the two-way *CW* pattern of *ADS*-based arrays are constrained to the values of

$\Theta(k, l)$

$$\left| S_{CW} \left(\frac{k}{s_x P}, \frac{l}{s_y Q} \right) \right|^2 = \Theta(k, l) \quad (10)$$

where

$$\Theta(k, l) \triangleq \begin{cases} K_T^2 (N - K_T)^2 & k = l = 0 \\ [K_T - \Lambda_T + \Psi(k, l)]^2 & \text{otherwise} \end{cases} \quad (11)$$

being $\Psi(0, 0) = N - 1 - t$ [18] and $K_T(K_T - 1) - t\Lambda_T = (\Lambda_T + 1)(N - 1 - t)$ [14]. Equation (10) points out that the samples of the two-way CW patterns of ADS -based arrays are *a-priori* known. Furthermore, by exploiting the sampling theorem [21], it can be shown that the two-way CW pattern of ADS -based arrays is equal to

$$\begin{aligned} |S_{CW}(u, v)|^2 &= \left| \sum_{k=0}^{P-1} \sum_{l=0}^{Q-1} \alpha_T(k, l) \frac{\sin(\pi s_x u P - k\pi)}{P \sin(\pi s_x u - \frac{k\pi}{P})} \frac{\sin(\pi s_y v Q - l\pi)}{Q \sin(\pi s_y v - \frac{l\pi}{Q})} \right|^2 \times \\ &\times \left| \sum_{k=0}^{P-1} \sum_{l=0}^{Q-1} \alpha_R(k, l) \frac{\sin(\pi s_x u P - k\pi)}{P \sin(\pi s_x u - \frac{k\pi}{P})} \frac{\sin(\pi s_y v Q - l\pi)}{Q \sin(\pi s_y v - \frac{l\pi}{Q})} \right|^2 \end{aligned} \quad (12)$$

where $\alpha_E(k, l)$, $E = T, R$, is the $IDFT$ of $a_E(p, q)$ related to $\Xi_E(k, l)$ by means of the circular correlation property [21]

$$\alpha_E(k, l) = \sqrt{\Xi_E(k, l)} e^{i\varphi_E(k, l)} \quad E = T, R. \quad (13)$$

As far as the peak sidelobe level of the two-way CW radiation pattern [1] is concerned, it is defined as the ratio between the maximum of the two-way CW pattern in the sidelobe region and the value of the two-way CW pattern in the steering direction u_0, v_0

$$PSL_{CW} \left[\mathbf{A}_{T/R}^{(\sigma_x, \sigma_y)} \right] \triangleq \frac{\max_{(u, v) \notin M_{CW}} \left| S_{CW}^{(\sigma_x, \sigma_y)}(u, v) \right|^2}{\left| S_{CW}^{(\sigma_x, \sigma_y)}(u_0, v_0) \right|^2}, \quad (14)$$

where M_{CW} is the two-way CW mainlobe region equal to the smallest region between M_T and M_R . Moreover, $\left| S_{CW}^{(\sigma_x, \sigma_y)}(u, v) \right|^2$ is the two-way CW pattern generated by $\mathbf{A}_T^{(\sigma_x, \sigma_y)}$ and $\mathbf{A}_R^{(\sigma_x, \sigma_y)}$. More specifically, by substituting (12) in (14) and using (13) and (11), one can obtain the following relation about the two-way radiation pattern of ADS -based designs

$$PSL_{CW} \left[\mathbf{A}_{T/R}^{(\sigma_x, \sigma_y)} \right] =$$

$$\begin{aligned}
& \max_{(u,v) \notin M_{CW}} \left\{ \left| \sum_{k=0}^{P-1} \sum_{l=0}^{Q-1} \frac{\sqrt{\Xi_T(k,l)} e^{i\varphi_T^{(\sigma_x, \sigma_y)}(k,l)} \sin(\pi s_x u P - k\pi) \sin(\pi s_y v Q - l\pi)}{P \sin\left(\pi s_x u - \frac{k\pi}{P}\right) Q \sin\left(\pi s_y v - \frac{l\pi}{Q}\right)} \right|^2 \times \right. \\
& \times \left. \left| \sum_{k=0}^{P-1} \sum_{l=0}^{Q-1} \frac{\sqrt{\Xi_R(k,l)} e^{i\varphi_R^{(\sigma_x, \sigma_y)}(k,l)} \sin(\pi s_x u P - k\pi) \sin(\pi s_y v Q - l\pi)}{P \sin\left(\pi s_x u - \frac{k\pi}{P}\right) Q \sin\left(\pi s_y v - \frac{l\pi}{Q}\right)} \right|^2 \right\} \frac{1}{[K_T^2 (N - K_T)^2]}. \quad (15)
\end{aligned}$$

As it can be noticed, PSL_{CW} is: (a) a function of $\Xi_E(k, l)$, $E = T, R$ given by (5) and (8) starting from the only knowledge of the *ADS* parameters [i.e., (N, K_T, Λ_T, t)]; (b) independent on the shift value (σ_x, σ_y) ; (c) a function of the phase terms $\varphi_E^{(\sigma_x, \sigma_y)}(k, l)$ computed through (13) once the explicit form of the *ADS* at hand is available [20]. Thanks to these properties, the following set of inequalities on the *PSL* of the two-way *CW* pattern of *ADS*-based arrays can be derived (see the Appendix)

$$PSL_{CW}^{INF} \leq PSL_{CW}^{MIN} \leq PSL_{CW}^{opt} \leq PSL_{CW}^{MAX} \leq PSL_{CW}^{SUP} \quad (16)$$

where $PSL_{CW}^{opt} \triangleq \min_{\sigma_x, \sigma_y} \left\{ PSL_{CW} \left[\mathbf{A}_{T/R}^{(\sigma_x, \sigma_y)} \right] \right\}$ and the upper and lower bounds are reported in Tab. I for the linear and planar cases, being $\Xi_E^{max} \triangleq \max_{(k,l) \notin \mathcal{H}_0} \{ \Xi_E(k, l) \}$, $\Xi_E^{min} \triangleq \min_{(k,l) \notin \mathcal{H}_0} \{ \Xi_E(k, l) \}$, $E = T, R$. As it can be noticed, the wider upper PSL_{CW}^{SUP} and lower bounds PSL_{CW}^{INF} are *a-priori* known only from the *ADS* features (N, K_T, Λ_T, t) , while the evaluation of the tighter bounds PSL_{CW}^{MIN} and PSL_{CW}^{MAX} requires the knowledge of the explicit form of the *ADS* at hand.

4 Numerical Analysis

In this section, the results of an extensive numerical study are presented to point out the features, the potentialities, and the limitations of *ADS*-based non-overlapping layouts as well as the reliability of the bounds in (16). Representative experiments concerned with different geometries (linear and planar) and aperture sizes are provided to investigate the two way *CW* response of *ADS* arrays and the accuracy of (16). Preliminary results on the pulsed-response properties of *ADS*-based layouts are discussed, as well.

The first test deals with arrays with $\nu = 0.5$. As regards the first experiment, the plot of

$PSL_{CW}(\mathbf{A}^{(\sigma)})$ in Fig. 3(a) refers to the linear layout derived from the (88, 44, 21, 22)-ADS ($N = P = 88, Q = 1, K_T = K_R = 44, \Lambda_T = \Lambda_R = 21, t = 22$ [20]) [Fig. 2(a)] and its shifted versions ($\sigma = 0, \dots, P - 1$). It points out that the peak sidelobe level in correspondence with $\sigma^{opt} \triangleq \arg \{ \min_{\sigma} [PSL_{CW}(\mathbf{A}^{(\sigma)})] \}$ (i.e. PSL_{CW}^{opt}) satisfies (16) as also confirmed by the two-way CW radiation pattern of $\mathbf{A}^{(\sigma^{opt})}$ [Fig. 2(b)]. As expected (10), $|S_{CW}(u)|^2$ exhibits a regular behavior for $u \notin M_{CW}$ since its samples are constrained to $\Theta(k, l)$ [Fig. 3(b)]. Moreover, Figure 3(a) also shows that different shifted arrangements derived from the same reference ADS provide PSL values within the bounds in (16) and always $PSL_{CW}^{INF} \leq PSL_{CW}(\mathbf{A}^{(\sigma)}) \leq PSL_{CW}^{SUP}$. This means that various configurations with good PSL performances can be obtained from a single ADS sequence.

The above considerations still hold true for larger linear arrays as highlighted by the second experiment related to the (700, 350, 174, 175)-ADS layout ($N = P = 700, Q = 1, K_T = K_R = 350, \Lambda_T = \Lambda_R = 174, t = 175$). Figure 4(a) shows the plot of $PSL_{CW}(\mathbf{A}^{(\sigma)})$, while the two-way CW pattern in correspondence with the optimal shift σ^{opt} is reported in Fig. 4(b). For completeness, Figure 5 summarizes the behavior of PSL_{CW}^{opt} versus the array aperture N when $\eta \triangleq \frac{t}{N-1} = 0.25$. As it can be observed, the value of PSL_{CW}^{opt} turns out to be quite close to the upper bound PSL_{CW}^{MAX} whatever the linear aperture size.

Dealing with planar geometries, Figures 6-8 are concerned with different-sized ADS layouts to further assess the general reliability of (10). More specifically, the following configurations have been analyzed: (49, 25, 12, 24)-ADS [Fig. 2(b) - Fig. 6], (529, 265, 132, 264)-ADS (Fig. 7), (1849, 1105, 552, 1104)-ADS (Fig. 8). The plots of $PSL_{CW}(\mathbf{A}^{(\sigma_x, \sigma_y)})$ [Figs. 6(a)-7(a)-8(a)] indicate, also for planar geometries, that multiple shifted arrays provide PSL values very close to PSL_{PE}^{opt} further pointing out the efficiency of the method in generating satisfactory solutions. Moreover, the behaviors of the optimal two-way CW patterns [Figs. 6(b)-7(b)-8(b)] show that the ADS arrays spread the radiation energy quite uniformly within the sidelobe region because of the pattern constraints at the sampling points (10). Finally, Figure 9 gives a summary of the performances of ADS-based arrays when $\nu = \eta = 0.5$ and for different dimensions of the square lattice ($P = Q = \sqrt{N}$). As expected, the main lobe width *monotonically* decreases with N and the same holds true for PSL_{CW}^{opt} .

Previous results are concerned with the *far-field* two-way *CW* response of *ADS* arrays. It is certainly a useful tool to evaluate the properties of an ultrasound array, since it represents a good approximation of the *CW* response in the focus of the array, as well as a first approximation of the pulsed response at a selected focal range or in the far field [1]. However the near-field pulse-echo response (i.e., the echo from a point-like target when excited by an incident pulse [1]) has also a great importance in several applications (e.g., biomedical imaging, underwater acoustic [1][22]). In order to provide some insights on the near-field pulse-echo properties of *ADS*-based arrangements, the steered pulse-echo responses of some *ADS*-based planar layouts have been simulated by using the program *Field II* [23][24] and the results compared with state-of-the-art designs [1][22]. For a fair comparison, planar arrays have been analyzed by assuming the same parameter setup of [1]: $c = 1540$ m/s (speed of sound), $f_0 = 3$ MHz (central frequency), $f_s = 102$ MHz (sampling frequency), $s_x = s_y = 0.6\lambda$ (element pitch), $\mathcal{F} = 40$ mm (focal range), an impulse response equal to a three-period sine with hamming weighting, and one period sine excitation.

For each simulation, the maximum projection function $W_{PE}(u, v)$ of the pulse-echo responses has been computed as well as the “worst-case cut” function $WC(\sin(\theta))$ [1]

$$WC(\sin(\theta)) \triangleq \max_{\phi \in [0, \pi]} \{W_{PE}(\sin(\theta) \cos(\phi), \sin(\theta) \sin(\phi))\}. \quad (17)$$

Moreover, the mainlobe beamwidth of $WC(\sin(\theta))$ at -6 , -20 and -50 dB (i.e., BW_6 , BW_{20} , BW_{50}) [1] has been evaluated along with the integrated sidelobe ratio (*ISLR*) defined as $ISLR \triangleq \frac{\int_{R_M} W_{PE}(u, v) du dv}{\int_{R_S} W_{PE}(u, v) du dv}$ [1][25][26] where $R_M \triangleq \{u, v \in [-1, 1] : u^2 + v^2 \leq BW_{50}\}$ and $R_S \triangleq \{u, v \in [-1, 1] : BW_{50} \leq u^2 + v^2 \leq 1\}$. The behavior of the largest peak in the angular range $\sin(\theta) \geq 0.2$, PSL_{NF} [1], has been analyzed, as well. It is worth pointing out that such descriptive parameters have been selected due to their importance in ultrasound imaging as a tool to investigate the obtainable contrast, noise-like artifacts, shadows, false targets and signal-to-noise ratio [1].

Filled/dense layouts [i.e., fully-overlapped: $a_T(p, q) = a_R(p, q) = 1$] have been considered as references since they are known to provide the best performances in ultrasound imaging applications even though with the highest hardware and processing costs [1].

By considering the optimal layout from the reference (49, 25, 12, 24)-*ADS* [Fig. 2(b)] and comparing the plot of $WC(\sin(\theta))$ along with the “worst case cut” of the corresponding 7×7 dense array [Fig. 10(a)], it turns out that the *ADS* solution provides performances similar to those of the square filled array in the neighborhood of the mainlobe, while a degradation can be observed when $|\sin(\theta)| \gtrsim 0.3$ [Fig. 10(a)]. The same considerations arise from the plots of $W_{PE}(u, v)$ [Figs. 10(b)-10(d)]. Moreover, the *ADS* synthesis provides a near-field pulse-echo pattern more regular in the sidelobe region. Since the *CW*-response provides a first approximation for $W_{PE}(u, v)$ [as pointed out by the plots in Fig. 6(b) and Fig. 10(b)], similar conclusions hold true also from the comparisons among the *CW*-responses of the corresponding layouts. For completeness, a uniform circular apodization has been applied to both the *ADS* layout and the filled arrangement since it generally improves the near-field ultrasound properties of planar transducer layouts [1][22]. The obtained results are reported in Fig. 10(a) in terms of $WC(\sin(\theta))$, while the associated $W_{PE}(u, v)$ functions are shown in Fig. 10(c) and Fig. 10(e). The circular apodization slightly affects the *ADS* radiation outside the mainlobe, while it significantly enhances the performances of the filled arrangement within the same angular region [Fig. 10(a)]. As for the near-field pulse-echo response, the modifications of the *ADS* pattern are limited [Fig. 10(b) vs. Fig. 10(c)], while its effect is more significant on the dense layout. As a matter of fact, a more uniform spread of the energy can be noticed within the sidelobe region [Fig. 10(d) vs. Fig. 10(e)]. The values of $ISLR$, PSL_{NF} , BW_6 , and BW_{20} reported in Tab. II together with the number of overlapping elements NC [$NC \triangleq \sum_{p=0}^{P-1} \sum_{q=0}^{Q-1} (a_T(p, q) \times a_R(p, q))$], the number of transmitters NT [$NT \triangleq \sum_{p=0}^{P-1} \sum_{q=0}^{Q-1} (a_T(p, q))$], and the number of receivers NR [$NR \triangleq \sum_{p=0}^{P-1} \sum_{q=0}^{Q-1} (a_R(p, q))$] further and quantitatively confirm the above outcomes. However, even for the filled layout, a very poor resolution is yielded (Tab. II) because of the small aperture.

In order to investigate more realistic configurations, the near-field behavior of the layouts coming from the (529, 265, 132, 264)-*ADS* and the (1849, 1105, 552, 1104)-*ADS* is analyzed hereinafter. The beamwidth of the radiated pattern is enhanced as pictorially show in Figs. 11(b)-12(b) and quantified by the corresponding indexes in Tab. II. Unlike the small array, the circular apodization tends now to improve the mainlobe width of *ADS*, as well [Figs. 11(a)-12(a) - Tab.

II]. On the other hand, even though the circular apodization enables a better distribution of the energy within the sidelobe region, the enhancement turns out to be less evident for *ADS*s [Fig. 11(c) vs. Fig. 11(e) and Fig. 12(c) vs. Fig. 12(e)] notwithstanding the decrease of PSL_{NF} [Tab. II]. Such an effect is due to the stronger impact of the reduction of the available elements on the non-overlapped layouts of the *ADS*s.

Because of the dimension of the *ADS*-layout in Fig. 12 similar to that considered in [1] (i.e., $N = 47 \times 47$ vs. $N = 48 \times 48$), the next analysis presents a comparison in terms of beamwidth, $ISLR$, and PSL_{NF} values with some reference designs in [1] (Tab. III). The values in Tab. II and Tab. III indicate that the beamwidths are quite similar for all considered designs, except for the dense square array whose mainlobe is wider due to the secondary lobes at $u = v = 0$ [Fig. 12(d)]. On the contrary, the values of $ISLR$ and PSL_{NF} exhibit non-negligible variations. More specifically, the lowest PSL_{NF} (except for the dense array) yielded with the ImpR4b architecture is of about 4 dB below that of the *ADS* layout, but its architecture presents a consistent number of overlapped channels ($NC_{ImpR4b} = 484$). On the contrary, non-overlapping or low overlapping designs (e.g., VERN, BIN, POL, and Rad4) give PSL_{NF} values significantly higher than that of the 47×47 *ADS* array (Tab. II), even though with a smaller number of active channels $NA = NT + NR$. Moreover, $ISLR$ values similar to that of the *ADS* displacement are exhibited by the VERN and Rad3 arrangements, while significantly improved $ISLR$ s are obtained only with strongly overlapped designs characterized by high NA values (e.g., Diag2, DP, DiagDP, and Dense architectures - Tab. III, Fig. 13(b)).

By sake of clarity, some representative points in the $(PSL_{NF}, ISLR)$ plane of the different layouts and various aperture sizes are reported in Fig. 13(a). More in detail, the BIN and POL designs have been taken into account since referred to non-overlapping layouts, while the VERN array has been analyzed for both the reduced number of overlapped elements ($NC = 48$ [1]) and its role as reference for ultrasound imaging [1][3]. The $N = 47 \times 47$ *ADS* array improves the $ISLR$ value of both the *BIN* and *POL* designs, while it turns out to be better than the *VERN* architecture in terms of PSL_{NF} . However, the *VERN* structure exhibits a smaller number of total active channels [$NA_{VERN} = 629$ vs. $NA_{ADS} = 1741$ for the apodized case - Fig. 13(b)]. One could also notice that the circularly apodized 23×23 *ADS* arrangement,

which has a lower NA ($NA_{ADS} = 421$), shows an improved PSL_{NF} and a similar $ISLR$ with respect to the 48×48 $VERN$ array (but a larger BW , due to the smaller aperture). As a matter of fact, only the $N = 48 \times 48$ circularly apodized layout [Fig. 13(a) - Tab. III] presents better radiation parameters than the ADS array defined over the same aperture, thanks to the overlapped texture, but at the cost of a significantly higher number of active channels [$NA_{DENSE} = 3608$ for the apodized case - Fig. 13(b)]. For completeness, Figure 13(a) also provides the results of other ADS designs in correspondence with wider and smaller apertures to point out that the circular apodization usually reduces the PSL_{NF} of ADS arrangements, while it does not substantially changes their $ISLR$. Moreover, the $ISLR$ value only slightly changes for larger aperture ADS s, while the PSL_{NF} value significantly reduces as N increases. These observations point out that ADS layouts provide a good tradeoff between the image contrast (which depends on the $ISLR$ [1]) and the resolution (i.e., BW) when compared to low- NC arrays when dealing with ultrasound imaging applications, while a significantly higher contrast can be achieved only with a more complex hardware (i.e., higher NC and NA) [Fig. 13(b)].

Finally, the capability of the proposed non-overlapped layouts to maintain the beam properties at different steering angles (θ_0, ϕ_0) is analyzed because its importance in ultrasound applications. Towards this end, the beam features of the 47×47 ADS -based array are evaluated for $\phi_0 = \frac{\pi}{4}$, $\theta_0 = -\frac{\pi}{4}, \dots, \frac{\pi}{4}$ and compared with those of the reference 47×47 dense array. The behaviour of PSL_{NF} , $ISLR$, and BW_{20} [Figs. 14(a)-14(c)], indicate that the figures of merit of the ADS s present, even for large steering angles, a dependency on θ_0 similar to that of dense arrangements despite the sparse nature of their layouts. More specifically, ADS s synthesize BW_{20} s almost identical to those of their filled counterparts [Fig. 14(c)] and a very similar PSL_{NF} especially for large values of θ_0 [Fig. 14(a)]. Moreover, unlike dense architectures, the arising $ISLR$ only slightly depends on θ_0 [Fig. 14(b)]. These features are confirmed by the plots of the steered $W_{PE}(u, v)$ for the 47×47 ADS -based array (Fig. 15 - $\phi_0 = \frac{\pi}{4}$, circular apodization). Indeed, the beam shape remains almost unaltered whatever the considered θ_0 [Fig. 15 - steered vs. Fig. 12(c) - unsteered], and no artifact appears in the steered pulsed response for small [$\theta_0 = \pm \frac{\pi}{12}$ - Figs. 15(a), 15(b)], medium [$\theta_0 = \pm \frac{\pi}{6}$ - 15(c), 15(d)], or large [$\theta_0 = \pm \frac{\pi}{4}$ - 15(e), 15(f)] steering

angles.

5 Conclusions

In this paper, an *ADS*-based methodology has been proposed to design non-overlapping transducer layouts for ultrasound imaging applications. The approach is not aimed at synthesizing optimal layouts, but rather to provide reliable general-purpose guidelines to efficiently design non-overlapping layouts with predictable and sub-optimal performances. An extensive numerical analysis has been carried out to assess the reliability of the *PSL* bounds as well as to evaluate the features of *ADS* designs in the *CW*/pulsed response cases and for both linear and planar geometries.

The obtained results have pointed out that

- the *ADS* approach can be profitably exploited to synthesize linear and planar non-overlapping arrangements;
- the optimal *PSL* of the far-field *CW*-response pattern of an *ADS*-based layout is *a-priori* bounded. Tighter bounds exist when the explicit form of the *ADS* sequence is available, otherwise larger bounds for PSL_{CW}^{opt} can be always determined from the only knowledge of the *ADS* features (i.e., N , K_T , Λ_T , t);
- the *ADS*-based methodology enables the design of arbitrary size arrays with negligible computational costs only related to simple shifts of the reference *ADS* sequence;
- several non-overlapping designs can be obtained from the reference *ADS* to comply different requirements on the radiated pattern;
- the near-field pulsed-response properties of *ADS* layouts favorably compare with those of reference state-of-the-art overlapping as well as non-overlapping designs in terms of both beamwidth, *ISLR*, and PSL_{NF} , even when large steering angles are at hand;
- the *ADS*-based technique can be used to define a suitable starting point for a local or a global search. In view of this, it can be easily and profitably integrated with state-of-the-

art optimization approaches for improving their rate of convergence and enabling their use in practical and large scale problems.

Future efforts will be aimed at providing *a-priori* estimates for the near-field performances of *ADS* arrangements, including their imaging capabilities with simulated ultrasound phantoms, as well as to deal with other array geometries and application scenarios. Finally, although out-of-the-scope of this present paper and outside current researches concerned with ultrasound imaging systems, but rather related to combinatorial mathematics, advances in *ADS* generation techniques are expected.

Acknowledgments

The authors wish to thank Prof. A. Austeng for his valuable suggestions and helpful comments. Moreover, the authors are grateful to the anonymous reviewers for their technical comments and suggestions.

Appendix

- *PSL bounds for ADS-based thinned linear and planar arrays*

Concerning linear *ADS* thinned arrays, the following bounds can be deduced [17]: $PSL_T^{INF} = \frac{K_T - \Lambda_T - 1 - \sqrt{\frac{t(N-t)}{(N-1)}}}{(N-1)\Lambda_T + K_T - 1 + N - t}$, $PSL_T^{MIN} = \max \left\{ \frac{[\max_{k \neq 0} \{\Xi_T(k)\}]}{K_T^2}, \frac{[\min_{k \neq 0} \{\Xi_T(k)\}][0.8488 + 1.128 \log_{10} N]}{K_T^2} \right\}$, $PSL_T^{MAX} = \frac{[\max_{k \neq 0} \{\Xi_T(k)\}][0.8488 + 1.128 \log_{10} N]}{K_T^2}$, and $PSL_T^{SUP} = [0.8488 + 1.128 \log_{10} N] \frac{K_T - \Lambda_T - 1 + \sqrt{t(N-t)}}{(N-1)\Lambda_T + K_T - 1 + N - t}$.

In such a case, the mainlobe region is defined as [17]

$$M_T = \left\{ - \left(2Nd \sqrt{\frac{\max_{k \neq 0} \Xi_T(k)}{\Xi_T(0)}} \right)^{-1} \leq u \leq \left(2Nd \sqrt{\frac{\max_{k \neq 0} \Xi_T(k)}{\Xi_T(0)}} \right)^{-1} \right\}. \quad (18)$$

As regards the planar case, the bounds on thinned *ADS* arrays turn out to be [18]: $PSL_T^{MIN} = \frac{[\min_{(k,l) \in \mathcal{H}_0} \{\Xi_T(k,l)\}][0.5 + 0.8 \log_{10}(PQ)]}{K^2}$, $PSL_T^{MAX} = \frac{[\max_{(k,l) \in \mathcal{H}_0} \{\Xi_T(k,l)\}][-0.1 + 1.5 \log_{10}(N)]}{K_T^2}$, $PSL_T^{INF} = \frac{K_T - \Lambda_T - \sqrt{\frac{(t+1)(N-1-t)}{N-1}}}{K_T^2}$, $PSL_T^{SUP} = \frac{(K_T - \Lambda_T + \sqrt{(t+1)(N-1-t)})[-0.1 + 1.5 \log_{10}(N)]}{K_T^2}$, where $\mathcal{H}_0 \triangleq \mathbf{G} \setminus (0,0)$.

In this case, the mainlobe region is given by [18]

$$M_T = \left\{ (u, v) \in [-1, 1] \times [-1, 1] : u^2 + v^2 \leq 1, uv \leq \frac{K_T}{4N s_x s_y \max_{(k,l) \in \mathcal{H}_0} |\Xi_T(k, l)|} \right\}. \quad (19)$$

- Derivation of PSL_{CW}^{SUP} in (16)

Let us first consider planar arrangements. With reference to the discrete version of $M_{CW} \triangleq \min \{M_T, M_R\}$ (19)

$$M_{CW}^D = \left\{ m, n \in \mathbb{Z}, \left(m + \frac{1}{2}\right) \left(n + \frac{1}{2}\right) \leq \min \left\{ \frac{K_T}{4 \max_{(k,l) \in \mathcal{H}_0} |\Xi_T(k, l)|}, \frac{K_R}{4 \max_{(k,l) \in \mathcal{H}_0} |\Xi_R(k, l)|} \right\} \right\}, \quad (20)$$

equation (15) is approximated as follows

$$PSL_{CW} \left[\mathbf{A}_{T/R}^{(\sigma_x, \sigma_y)} \right] \approx \max_{(m,n) \notin M_{CW}^D} \left\{ \left| \sum_{k=0, kl \neq 0}^{P-1} \sum_{l=0, kl \neq 0}^{Q-1} \frac{\sqrt{\Xi_T(k, l)} e^{i\varphi_T^{(\sigma_x, \sigma_y)}(k, l)} (-1)^{m+n-k-l}}{N \sin\left[\frac{\pi}{P}\left(m-k+\frac{1}{2}\right)\right] \sin\left[\frac{\pi}{Q}\left(n-l+\frac{1}{2}\right)\right]} \right|^2 \times \right. \\ \left. \times \left| \sum_{k=0, kl \neq 0}^{P-1} \sum_{l=0, kl \neq 0}^{Q-1} \frac{\sqrt{\Xi_R(k, l)} e^{i\varphi_R^{(\sigma_x, \sigma_y)}(k, l)} (-1)^{m+n-k-l}}{N \sin\left[\frac{\pi}{P}\left(m-k+\frac{1}{2}\right)\right] \sin\left[\frac{\pi}{Q}\left(n-l+\frac{1}{2}\right)\right]} \right|^2 \right\} / [K_T^2 (N - K_T)^2] \quad (21)$$

by neglecting the term at $k = l = 0$ since the “max” operator is applied in the sidelobe region [18]. To define an upper bound for PSL_{CW} , let us notice that (5)

$$\max_{(k,l) \notin \mathcal{H}_0} \{\Xi_T(k, l)\} = K_T - \Lambda_T + \max_{(k,l) \notin \mathcal{H}_0} \{\Psi(k, l)\}. \quad (22)$$

By applying the Parseval’s theorem to the real valued function $\Psi(k, l)$, it can be obtained that $\sum_{p=0}^{P-1} \sum_{q=0}^{Q-1} [\Psi(k, l)]^2 = N(N-1-t)$. Moreover, since $\Psi(0, 0) = N-1-t$, it turns out that $\max_{(k,l) \notin \mathcal{H}_0} \{\Psi(k, l)\} \leq \sqrt{(t+1)(N-1-t)}$. Therefore

$$\max_{(k,l) \notin \mathcal{H}_0} \{\Xi_T(k, l)\} \leq K_T - \Lambda_T + \sqrt{(t+1)(N-1-t)}. \quad (23)$$

[a similar expression can be determined for $\Xi_R(k, l)$ by using (8)]. By substituting (23) in (30),

it results that

$$\begin{aligned}
PSL_{CW} \left[\mathbf{A}_{T/R}^{(\sigma_x, \sigma_y)} \right] &\leq \frac{\left[K_T - \Lambda_T + \sqrt{(t+1)(N-1-t)} \right] \left[K_R - \Lambda_R + \sqrt{(t+1)(N-1-t)} \right]}{\left[K_T^2 (N - K_T)^2 \right]} \times \\
&\max_{(m,n) \notin M_{CW}^D} \left\{ \left| \sum_{k=0, k \neq 0}^{P-1} \sum_{l=0, k \neq 0}^{Q-1} \frac{e^{i\varphi_T^{(\sigma_x, \sigma_y)}(k,l)} (-1)^{m+n-k-l}}{N \sin \left[\frac{\pi}{P} \left(m - k + \frac{1}{2} \right) \right] \sin \left[\frac{\pi}{Q} \left(n - l + \frac{1}{2} \right) \right]} \right|^2 \times \right. \\
&\left. \times \left| \sum_{k=0, k \neq 0}^{P-1} \sum_{l=0, k \neq 0}^{Q-1} \frac{e^{i\varphi_R^{(\sigma_x, \sigma_y)}(k,l)} (-1)^{m+n-k-l}}{N \sin \left[\frac{\pi}{P} \left(m - k + \frac{1}{2} \right) \right] \sin \left[\frac{\pi}{Q} \left(n - l + \frac{1}{2} \right) \right]} \right|^2 \right\}. \tag{24}
\end{aligned}$$

In analogy with [18][16], let us treat the phase terms $\varphi_T^{(\sigma_x, \sigma_y)}(k, l)$ and $\varphi_R^{(\sigma_x, \sigma_y)}(k, l)$, although deterministic, as independently identically distributed uniform random variables to rewrite (24) as

$$PSL_{CW}^{opt} \leq \Upsilon \frac{\left[K_T - \Lambda_T + \sqrt{(t+1)(N-1-t)} \right] \left[K_R - \Lambda_R + \sqrt{(t+1)(N-1-t)} \right]}{\left[K_T^2 (N - K_T)^2 \right]} \tag{25}$$

where $\Upsilon \triangleq \min_{(\sigma_x, \sigma_y)} \{ \max \{ H_0, \dots, H_{C-1} \} \}$, $C \approx N$ is the cardinality of M_{CW}^D , and $H_i \triangleq \left[\left| \sum_{k=-\infty}^{\infty} \sum_{l=-\infty}^{\infty} \frac{e^{i\varphi_T^{(\sigma_x, \sigma_y)}(k,l)}}{\pi^2 (k-\frac{1}{2})(l-\frac{1}{2})} \right|^2 \times \left| \sum_{k=-\infty}^{\infty} \sum_{l=-\infty}^{\infty} \frac{e^{i\varphi_R^{(\sigma_x, \sigma_y)}(k,l)}}{\pi^2 (k-\frac{1}{2})(l-\frac{1}{2})} \right|^2 \right]$, $i = 0, \dots, C-1$. Since the statistics of Υ are not available in closed form, its mean value can be approximated as follows

$$E \{ \Upsilon \} \approx [-0.1 + 1.5 \log_{10} (N)]^2. \tag{26}$$

Finally, the upper bound PSL_{CW}^{SUP} is then obtained by substituting (26) in (25).

Starting from (15) and setting $Q = 1$, PSL_{CW}^{SUP} for linear arrays can be derived by following the same procedure detailed above when dealing with planar architectures.

- Derivation of PSL_{CW}^{INF} in (16)

As regards planar layouts and considering the sampled version of (15) at $u = \frac{f}{Ps_x}$, $f = 0, \dots, P-1$, $v = \frac{g}{Qs_y}$, $g = 0, \dots, Q-1$, it can be deduced that

$$PSL_{CW}^{opt} \geq PSL_{CW} \left[\mathbf{A}_{T/R}^{(\sigma_x, \sigma_y)} \right] \Big|_{u=\frac{f}{Ps_x}, v=\frac{g}{Qs_y}} = \frac{\max_{(f,g) \in \mathcal{H}_0} \{ \Xi_T(k, l) \times \Xi_R(k, l) \}}{K_T^2 (N - K_T)^2}. \tag{27}$$

The lower bound PSL_{CW}^{INF} is then obtained

$$PSL_{CW}^{INF} = \left[\frac{K_T - \Lambda_T - \sqrt{\frac{(t+1)(N-1-t)}{N-1}}}{K_T(N - K_T)} \right]^2 \quad (28)$$

by exploiting (27), (22), and observing that $\max_{(k,l) \in \mathcal{H}_0} \{\Psi(k, l)\} \geq -\sqrt{\frac{(t+1)(N-1-t)}{N-1}}$.

A similar procedure applies to the linear case, as well.

- Derivation of PSL_{CW}^{MAX} in (16)

With reference to (30) and still considering the planar case for generality, let us observe that $\Xi_T^{max} \triangleq \max_{(k,l) \notin \mathcal{H}_0} \{\Xi_T(k, l)\}$ and $\Xi_R^{max} \triangleq \max_{(k,l) \notin \mathcal{H}_0} \{\Xi_R(k, l)\}$ are known quantities when the explicit form of the ADS at hand is available. Equation (30) can be then rewritten as

$$PSL_{CW} \left[\mathbf{A}_{T/R}^{(\sigma_x, \sigma_y)} \right] \leq \Xi_T^{max} \Xi_R^{max} \max_{(m,n) \notin M_{CW}^D} \left\{ \left| \sum_{k=0, kl \neq 0}^{P-1} \sum_{l=0, kl \neq 0}^{Q-1} \frac{e^{i\varphi_T^{(\sigma_x, \sigma_y)}(k,l)} (-1)^{m+n-k-l}}{N \sin\left[\frac{\pi}{P}\left(m-k+\frac{1}{2}\right)\right] \sin\left[\frac{\pi}{Q}\left(n-l+\frac{1}{2}\right)\right]} \right|^2 \times \right. \\ \left. \times \left| \sum_{k=0, kl \neq 0}^{P-1} \sum_{l=0, kl \neq 0}^{Q-1} \frac{e^{i\varphi_R^{(\sigma_x, \sigma_y)}(k,l)} (-1)^{m+n-k-l}}{N \sin\left[\frac{\pi}{P}\left(m-k+\frac{1}{2}\right)\right] \sin\left[\frac{\pi}{Q}\left(n-l+\frac{1}{2}\right)\right]} \right|^2 \right\} / [K_T^2 (N - K_T)^2]. \quad (29)$$

By dealing with the phase terms as random variables, it turns out that

$$PSL_{CW}^{opt} \leq \frac{\Upsilon \Xi_T^{max} \Xi_R^{max}}{K_T^2 (N - K_T)^2}$$

and the upper bound PSL_{CW}^{MAX} is finally derived through (26).

- Derivation of PSL_{CW}^{MIN} in (16)

As regards two-dimensional layouts and using (30), one can deduce that

$$PSL_{CW}^{opt} \gtrsim \Xi_T^{min} \Xi_R^{min} \min_{(\sigma_x, \sigma_y)} \left\{ \max_{(m,n) \notin M_{CW}^D} \left[\left| \sum_{k=0, kl \neq 0}^{P-1} \sum_{l=0, kl \neq 0}^{Q-1} \frac{e^{i\varphi_T^{(\sigma_x, \sigma_y)}(k,l)} (-1)^{m+n-k-l}}{N \sin\left[\frac{\pi}{P}\left(m-k+\frac{1}{2}\right)\right] \sin\left[\frac{\pi}{Q}\left(n-l+\frac{1}{2}\right)\right]} \right|^2 \right. \right. \\ \left. \left. \times \left| \sum_{k=0, kl \neq 0}^{P-1} \sum_{l=0, kl \neq 0}^{Q-1} \frac{e^{i\varphi_R^{(\sigma_x, \sigma_y)}(k,l)} (-1)^{m+n-k-l}}{N \sin\left[\frac{\pi}{P}\left(m-k+\frac{1}{2}\right)\right] \sin\left[\frac{\pi}{Q}\left(n-l+\frac{1}{2}\right)\right]} \right|^2 \right] \right\} / [K_T^2 (N - K_T)^2] \quad (30)$$

where $\Xi_E^{min} \triangleq \min_{(k,l) \notin \mathcal{H}_0} \{\Xi_E(k,l)\}$, $E = T, R$, is a known quantity when the *ADS* at hand is known. By dealing with the random representation of the phase terms and taking into account that, in this case, the summations cannot be extended to $\pm\infty$, the following approximation holds true

$$PSL_{CW}^{opt} \gtrsim \frac{\Xi_T^{min} \Xi_R^{min} [0.5 + 0.8 \log_{10} N]^2}{K_T^2 (N - K_T)^2}.$$

PSL_{CW}^{MIN} is then defined as the right term of previous expression.

Dealing with linear arrangements, PSL_{CW}^{MIN} can be simply obtained by substituting the known quantities Ξ_T^{max} and Ξ_R^{max} in (27) to Ξ_T^{min} and Ξ_R^{min} .

References

- [1] A. Austeng and S. Holm, "Sparse 2-D arrays for 3-D phased array imaging - design methods," *IEEE Trans. Ultrason., Ferroelectr., Freq. Control*, vol. 49, no. 8, pp. 1073-1086, Aug. 2002.
- [2] M. Karaman, I. O. Wygant, O. Oralkan, and B. T. Khuri-Yakob, "Minimally redundant 2-D array designs for 3-D Medical Ultrasound Imaging", *IEEE Trans. Med. Imag.*, vol. 28, no. 7, pp. 1051-1061, Jul. 2009.
- [3] G. R. Lockwood, P.-C. Li, M. O'Donnell, and F. S. Foster, "Optimizing the radiation pattern of sparse periodic linear arrays," *IEEE Trans. Ultrason., Ferroelectr., Freq. Control*, vol. 43, no. 1, pp. 7-14, Jan. 1996.
- [4] A. Trucco, E. Omodei, P. Repetto, "Synthesis of Sparse Planar Arrays," *Electronics Letters*, vol. 33, no. 22, pp. 1834-1835, 23rd October 1997.
- [5] A. Trucco and V. Murino, "Stochastic optimization of linear sparse arrays," *IEEE J. Ocean Eng.*, vol. 24, no. 3, pp. 291-299, Jul. 1999.
- [6] A. Trucco, "Synthesising Asymmetric Beam Patterns," *IEEE Journal of Oceanic Engineering*, vol. 25, no. 3, pp. 347-350, July 2000.

- [7] A. Trucco, "Weighting and Thinning Wide-Band Arrays by Simulated Annealing," *Ultrasonics*, vol. 40, no. 1-8, pp. 485-489, March 2002
- [8] D. H. Turnbull and F. S. Foster, "Beam steering with pulsed two-dimensional transducer arrays," *IEEE Trans. Ultrason., Ferroelectr., Freq. Control*, vol. 38, no. 4, pp. 320-333, Jul. 1991.
- [9] G. R. Lockwood and F. S. Foster, "Optimizing the radiation pattern of sparse periodic two-dimensional arrays," *IEEE Trans. Ultrason., Ferroelectr., Freq. Control*, vol. 43, no. 1, pp. 15-19, Jan. 1996.
- [10] P. K. Weber, R. M. Schmitt, B. D. Tylkowski, and J. Steck, "Optimization of random sparse 2-D transducer arrays for 3-D electronic beam steering and focusing", in *Proc. IEEE Ultrason. Symp.*, vol. 3, pp. 1503-1506, 1994.
- [11] S. Holm, B. Elgetun, and G. Dahl, "Properties of the beampattern of weight- and layout-optimized sparse arrays," *IEEE Trans. Ultrason., Ferroelectr., Freq. Control*, vol. 44, no. 5, pp. 983-991, Sep. 1997.
- [12] A. Trucco, "Thinning and weighting of large planar arrays by simulated annealing," *IEEE Trans. Ultrason., Ferroelectr., Freq. Control*, vol. 46, no. 2, pp. 347-355, Mar. 1999.
- [13] C. Ding, T. Helleseth, and K. Y. Lam, "Several classes of binary sequences with three-level autocorrelation," *IEEE Trans. Inf. Theory*, vol. 45, no. 7, pp. 2606-2612, Nov. 1999.
- [14] K. T. Arasu, C. Ding, T. Helleseth, P. V. Kumar, and H. M. Martinsen, "Almost difference sets and their sequences with optimal autocorrelation," *IEEE Trans. Inf. Theory*, vol. 47, no. 7, pp. 2934-2943, Nov. 2001.
- [15] Y. Zhang, J. G. Lei, and S. P. Zhang, "A new family of almost difference sets and some necessary conditions," *IEEE Trans. Inf. Theory*, vol. 52, no. 5, pp. 2052-2061, May 2006.
- [16] D. G. Leeper, "Isophoric arrays - massively thinned phased arrays with well-controlled sidelobes," *IEEE Trans. Antennas Propag.*, vol. 47, no. 12, pp. 1825-1835, Dec. 1999.

- [17] G. Oliveri, M. Donelli, and A. Massa, "Linear array thinning exploiting almost difference sets," *IEEE Trans. Antennas Propag.*, vol. 57, no. 12, pp. 3800-3812, Dec. 2009.
- [18] G. Oliveri, L. Manica, and A. Massa, "ADS-based guidelines for thinned planar arrays," *IEEE Trans. Antennas Propag.*, in press.
- [19] C. A. Balanis, *Antenna Theory: Analysis and Design*, 2nd ed. New York: Wiley, 1997.
- [20] ELEDIA Almost Difference Set Repository (<http://www.eledia.ing.unitn.it/>).
- [21] J. G. Proakis and D. G. Manolakis, *Digital Signal Processing: Principles, Algorithms, and Applications*, 3rd ed. London: Prentice Hall, 1996.
- [22] A. Austeng and S. Holm, "Sparse 2-D arrays for 3-D phased array imaging - experimental validation," *IEEE Trans. Ultrason., Ferroelectr., Freq. Control*, vol. 49, no. 8, pp. 1087-1093, Aug. 2002.
- [23] J. A. Jensen and N. B. Svendsen, "Calculation of pressure fields from arbitrarily shaped, apodized, and excited ultrasound transducers", *IEEE Trans. Ultrason., Ferroelec., Freq. Contr.*, Vol. 39, no. 2, pp. 262-267, Mar. 1992.
- [24] J. A. Jensen, "Field: a program for simulating ultrasound systems," in *10th Nordic-Baltic Conf. Biomed. Imag., Med. Biol. Eng. Comput.*, vol. 34, Suppl. 1, p. 1, pp. 351-353, 1996.
- [25] C. Boni, M. Richards, and S. Barbarossa, "Optimal configuration and weighting of nonuniform arrays according to a maximum ISLR criterion," in *IEEE Int. Conf. Acoust., Speech, Sign. Proc.*, vol. V, pp. 157-160, 1994.
- [26] S. Holm, "Minimum sidelobe energy versus minimum peak sidelobe level for sparse array optimization," in *Proc. IEEE Nordic Sign. Proc. Symposium*, pp. 227-230, Sep. 1996.

FIGURE CAPTIONS

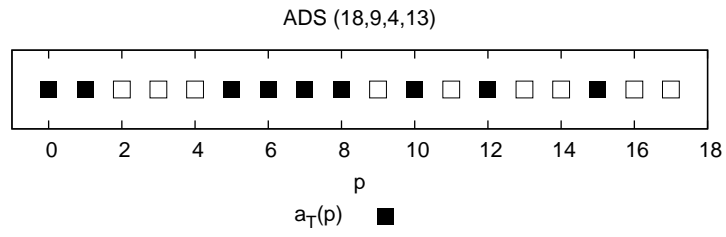
- **Figure 1.** *ADS* thinned array layout obtained from the (18, 9, 4, 13)-*ADS* ($P = 18$, $Q = 1$) [20] (a) and associated autocorrelation (b) and beam pattern (c) properties.
- **Figure 2.** Non-overlapping *ADS* layouts obtained from (a) the (88, 44, 21, 22)-*ADS* ($P = 88$, $Q = 1$) [20] and (b) the (49, 25, 12, 24)-*ADS* ($P = Q = 47$) [20].
- **Figure 3.** *Far-field CW-response properties - Linear Array* (88, 44, 21, 22)-*ADS* [20]: (a) $PSL_{CW}(\mathbf{A}^{(\sigma)})$ values versus $\sigma = 0, \dots, N-1$ and (b) plot of the normalized $|S_{CW}(u)|^2$ in correspondence with σ^{opt} . Aperture size: 43.5λ .
- **Figure 4.** *Far-field CW-response properties - Linear Array* (700, 350, 174, 175)-*ADS* [20]: (a) $PSL_{CW}(\mathbf{A}^{(\sigma)})$ values versus $\sigma = 0, \dots, N-1$ and (b) plot of the normalized $|S_{CW}(u)|^2$ in correspondence with σ^{opt} . Aperture size: 349.5λ .
- **Figure 5.** *Far-field CW-response properties - Linear Arrays.* Plots of the PSL_{CW}^{opt} values and associated bounds for *ADS*-based linear arrangements when $\nu = 0.5$ and $\eta = 0.25$.
- **Figure 6.** *Far-field CW-response properties - Planar Array* (49, 25, 12, 24)-*ADS* [20]: (a) $PSL_{CW}(\mathbf{A}^{(\sigma_x, \sigma_y)})$ values versus $\sigma_x = 0, \dots, P-1$, $\sigma_y = 0, \dots, Q-1$ and (b) plot of the normalized $|S_{CW}(u, v)|^2$ in correspondence with σ^{opt} . Aperture size: $3\lambda \times 3\lambda$.
- **Figure 7.** *Far-field CW-response properties - Planar Array* (529, 265, 132, 264)-*ADS* [20]: (a) $PSL_{CW}(\mathbf{A}^{(\sigma_x, \sigma_y)})$ values versus $\sigma_x = 0, \dots, P-1$, $\sigma_y = 0, \dots, Q-1$ and (b) plot of the normalized $|S_{CW}(u, v)|^2$ in correspondence with σ^{opt} . Aperture size: $11\lambda \times 11\lambda$.
- **Figure 8.** *Far-field CW-response properties - Planar Array* (2209, 1105, 552, 1104)-*ADS* [20]: (a) $PSL_{CW}(\mathbf{A}^{(\sigma_x, \sigma_y)})$ values versus $\sigma_x = 0, \dots, P-1$, $\sigma_y = 0, \dots, Q-1$ and (b) plot of the normalized $|S_{CW}(u, v)|^2$ in correspondence with σ^{opt} . Aperture size: $23\lambda \times 23\lambda$.
- **Figure 9.** *Far-field CW-response properties - Planar Arrays.* Plots of the PSL_{CW}^{opt} values and associated bounds for *ADS*-based planar arrangements when $\nu = 0.5$ and $\eta = 0.5$.

- **Figure 10.** *Near-field pulsed-response properties - Planar Arrays* ($N = 7 \times 7$). (a) Plots of $WC(\sin(\theta))$ for different non-overlapping/dense arrays with uniform/circular apodization and plot of the normalized $W_{PE}(u, v)$ in correspondence with: (b) $\mathbf{A}^{(\sigma_x^{opt}, \sigma_y^{opt})}$ [(49, 25, 12, 24)-ADS] - Uniform apodization, (c) $\mathbf{A}^{(\sigma_x^{opt}, \sigma_y^{opt})}$ [(49, 25, 12, 24)-ADS] - Circular apodization, (d) Dense layout $N = 7 \times 7$ - Uniform apodization, and (e) Dense layout $N = 7 \times 7$ - Circular apodization. Aperture size: $3\lambda \times 3\lambda$.
- **Figure 11.** *Near-field pulsed-response properties - Planar Arrays* ($N = 23 \times 23$). (a) Plots of $WC(\sin(\theta))$ for different non-overlapping/dense arrays with uniform/circular apodization and plot of the normalized $W_{PE}(u, v)$ in correspondence with: (b) $\mathbf{A}^{(\sigma_x^{opt}, \sigma_y^{opt})}$ [(529, 265, 132, 264)-ADS] - Uniform apodization, (c) $\mathbf{A}^{(\sigma_x^{opt}, \sigma_y^{opt})}$ [(529, 265, 132, 264)-ADS] - Circular apodization, (d) Dense layout $N = 23 \times 23$ - Uniform apodization, and (e) Dense layout $N = 23 \times 23$ - Circular apodization. Aperture size: $11\lambda \times 11\lambda$.
- **Figure 12.** *Near-field pulsed-response properties - Planar Arrays* ($N = 47 \times 47$). (a) Plots of $WC(\sin(\theta))$ for different non-overlapping/dense arrays with uniform/circular apodization and plot of the normalized $W_{PE}(u, v)$ in correspondence with: (b) $\mathbf{A}^{(\sigma_x^{opt}, \sigma_y^{opt})}$ [(2209, 1105, 552, 1104)-ADS] - Uniform apodization, (c) $\mathbf{A}^{(\sigma_x^{opt}, \sigma_y^{opt})}$ [(2209, 1105, 552, 1104)-ADS] - Circular apodization, (d) Dense layout $N = 47 \times 47$ - Uniform apodization, and (e) Dense layout $N = 47 \times 47$ - Circular apodization. Aperture size: $23\lambda \times 23\lambda$.
- **Figure 13.** *Near-field pulsed-response properties - Planar Arrays.* Plots of (a) PSL_{NF} [dB] versus $ISLR$ [dB] and (b) PSL_{NF} [dB] and $ISLR$ [dB] versus NA for ADS arrays [$P = Q$; (a) $P = 17, 23, 31, 47, 61, 71$; (b) $P = 47$] with uniform and circular apodization and representative samples of reference layouts [1].
- **Figure 14.** *Near-field pulsed-response properties - Planar Arrays* ($\phi_0 = \frac{\pi}{4}$ [rad]). Behaviour of PSL_{NF} [dB] (a), $ISLR$ [dB] (b), and BW_{20} [deg] (c) versus steering angle θ_0 for ADS arrays [$P = Q = 47$] and for reference filled layouts, with uniform and circular apodization.
- **Figure 15.** *Near-field pulsed-response properties - Planar Arrays* ($\phi_0 = \frac{\pi}{4}$ [rad]). Plot of the normalized $W_{PE}(u, v)$ in correspondence with $\mathbf{A}^{(\sigma_x^{opt}, \sigma_y^{opt})}$ [(2209, 1105, 552, 1104)-

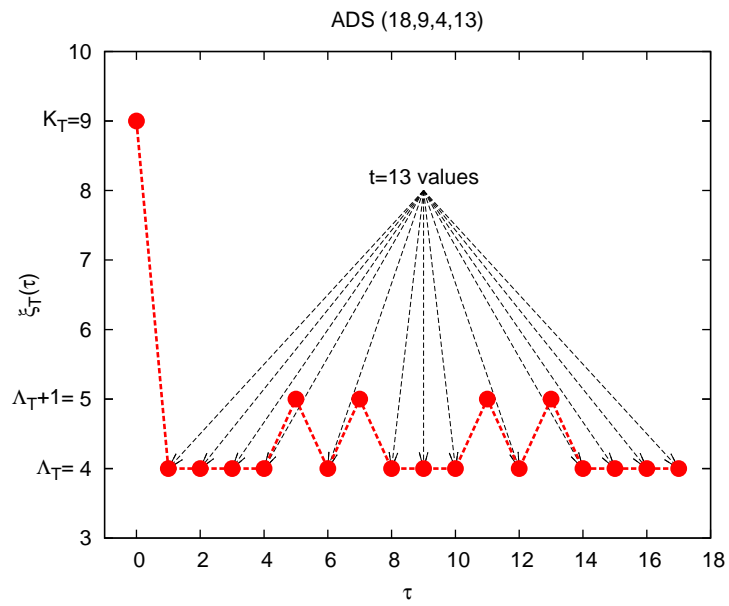
ADS] with circular apodization for (a) $\theta_0 = -\frac{\pi}{4}$, (b) $\theta_0 = \frac{\pi}{4}$, (c) $\theta_0 = -\frac{\pi}{6}$, (d) $\theta_0 = \frac{\pi}{6}$, (e) $\theta_0 = -\frac{\pi}{12}$, (f) $\theta_0 = \frac{\pi}{12}$.

TABLE CAPTIONS

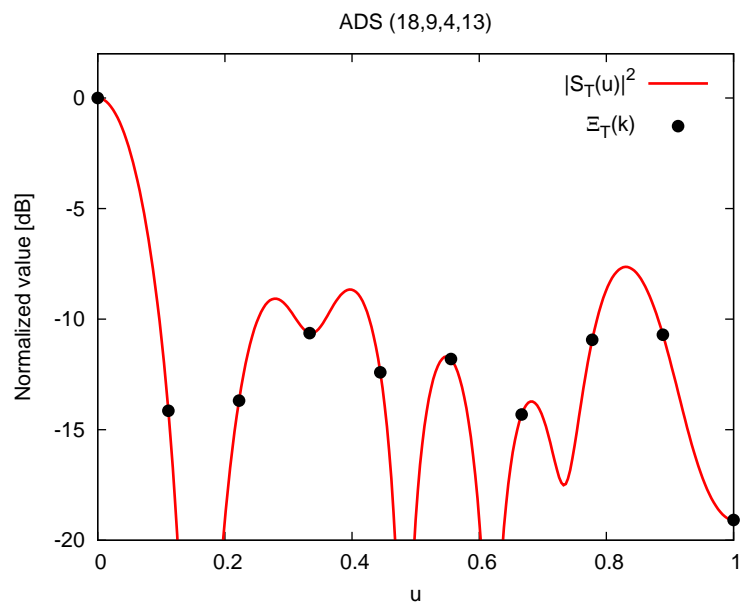
- **Table I.** *Far-field CW-response properties.* Closed-form expressions for the *PSL* bounds of *ADS*-based layouts.
- **Table II.** *Near-field pulsed-response properties - Planar Arrays* [$P = Q$, $P = 7, 23, 47$]. Values of the descriptive indexes (*BW*, *ISLR*, *PSL_{NF}*).
- **Table III.** *Near-field pulsed-response properties - Planar Arrays* [$P = Q = 48$]. Values of the descriptive indexes (*BW*, *ISLR*, *PSL_{NF}*).



(a)



(b)



(c)

Figure 1 - G. Oliveri et al., “ADS-based Array Design for 2D and 3D Ultrasound Imaging”

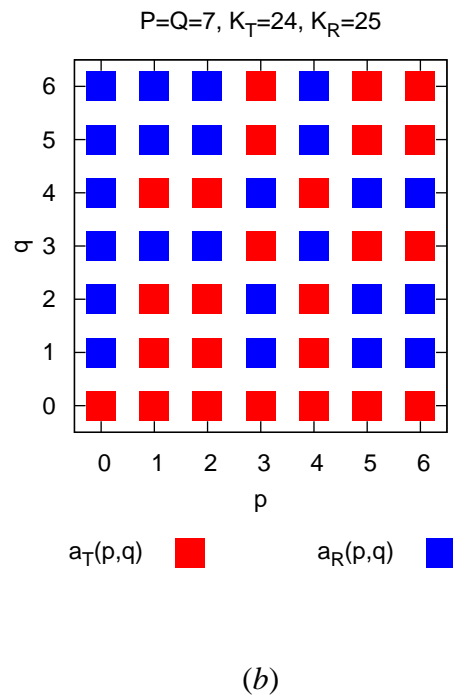
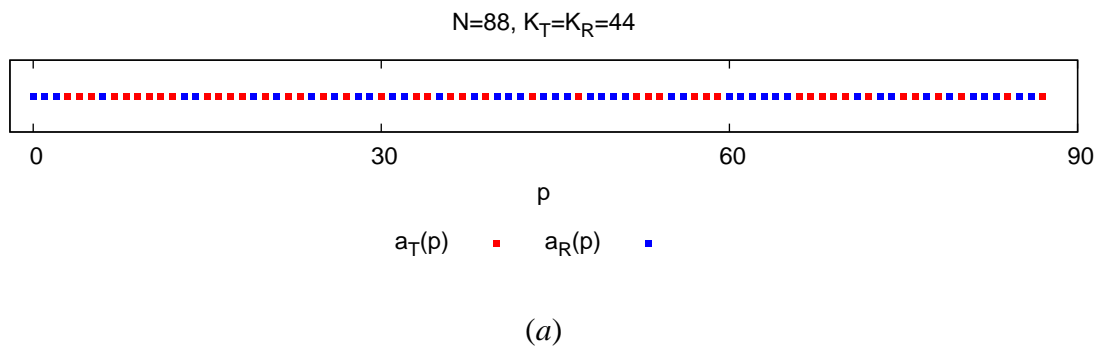
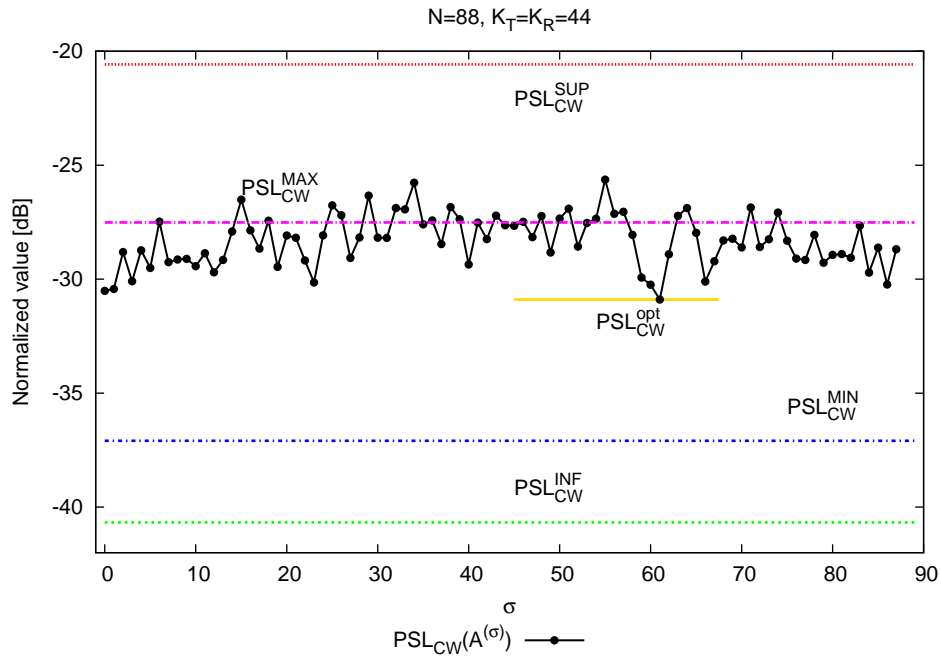
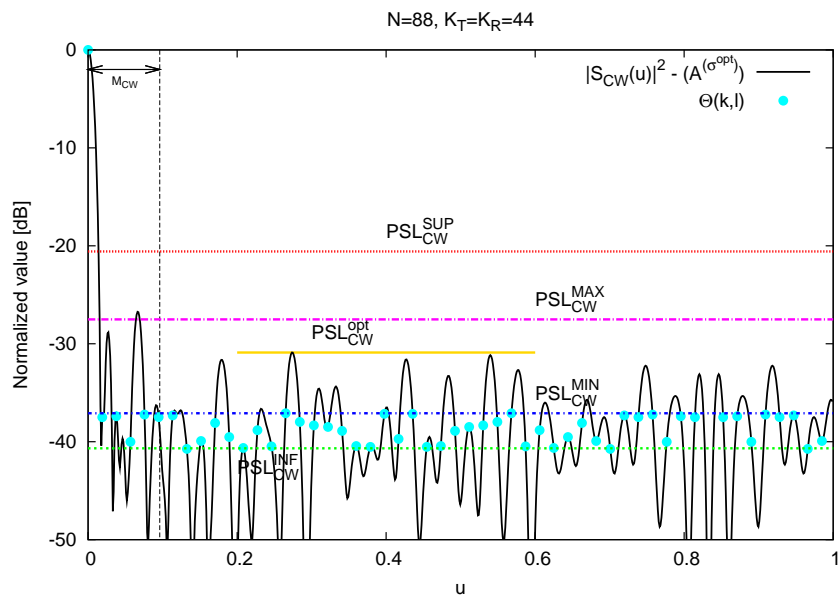


Figure 2 - G. Oliveri et al., “ADS-based Array Design for 2D and 3D Ultrasound Imaging”



(a)



(b)

Figure 3 - G. Oliveri et al., “ADS-based Array Design for 2D and 3D Ultrasound Imaging”

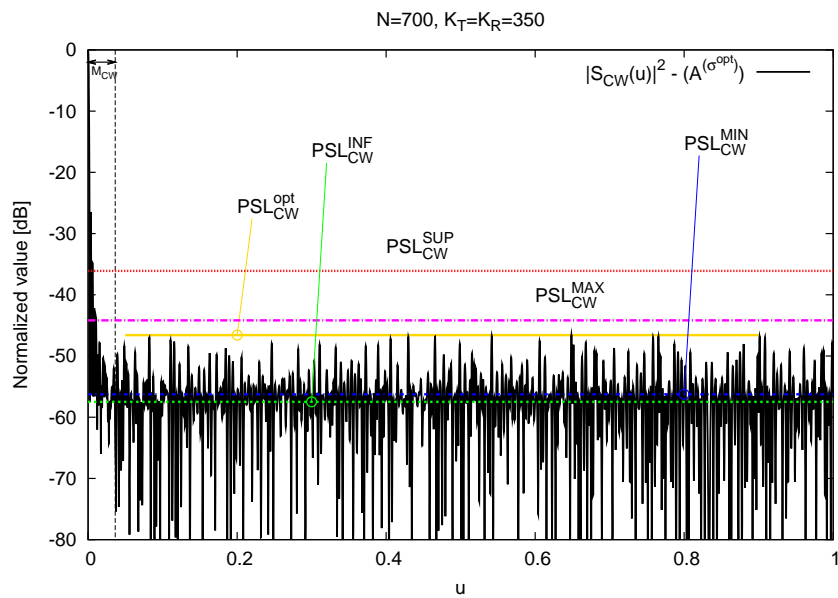
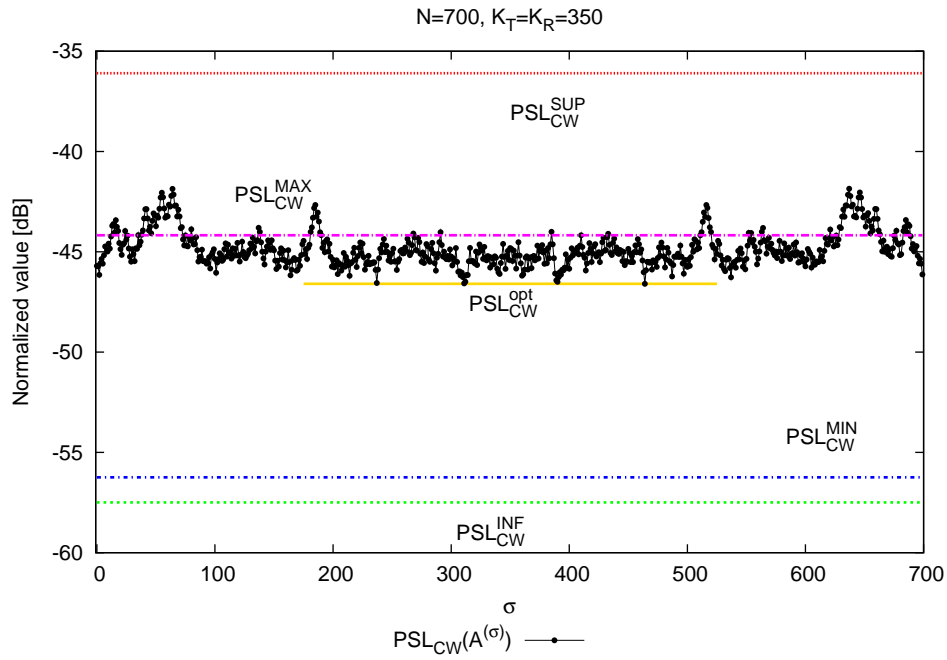


Figure 4 - G. Oliveri et al., “ADS-based Array Design for 2D and 3D Ultrasound Imaging”

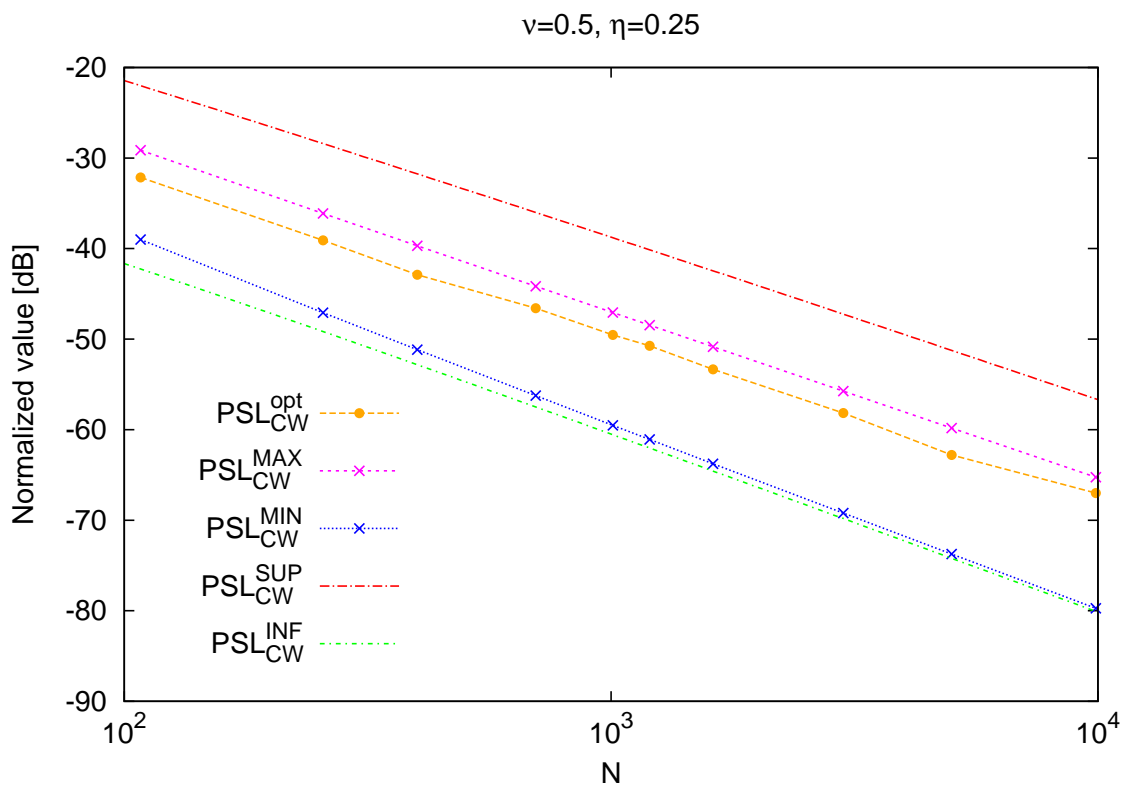
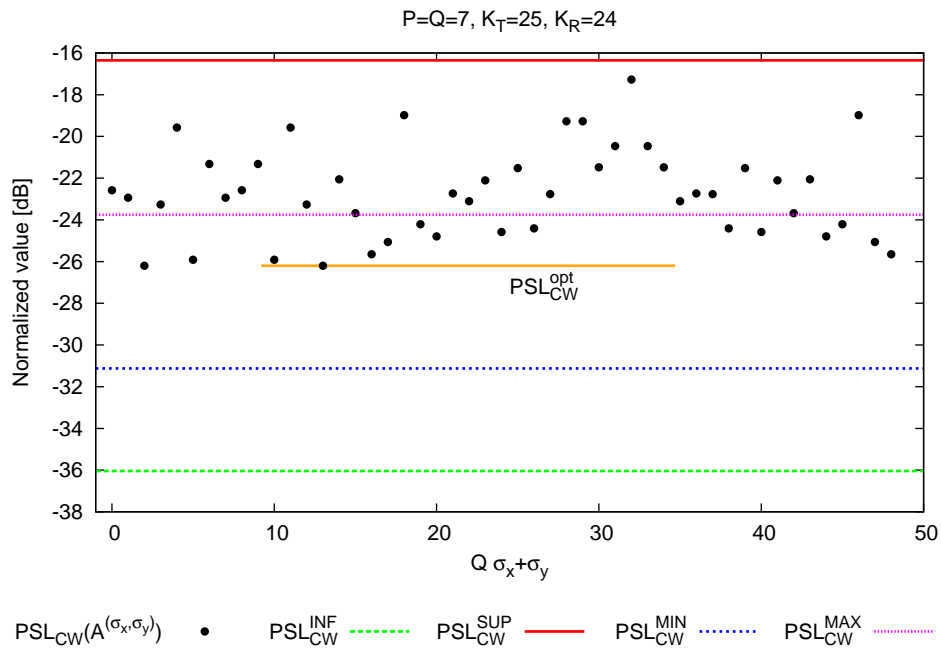
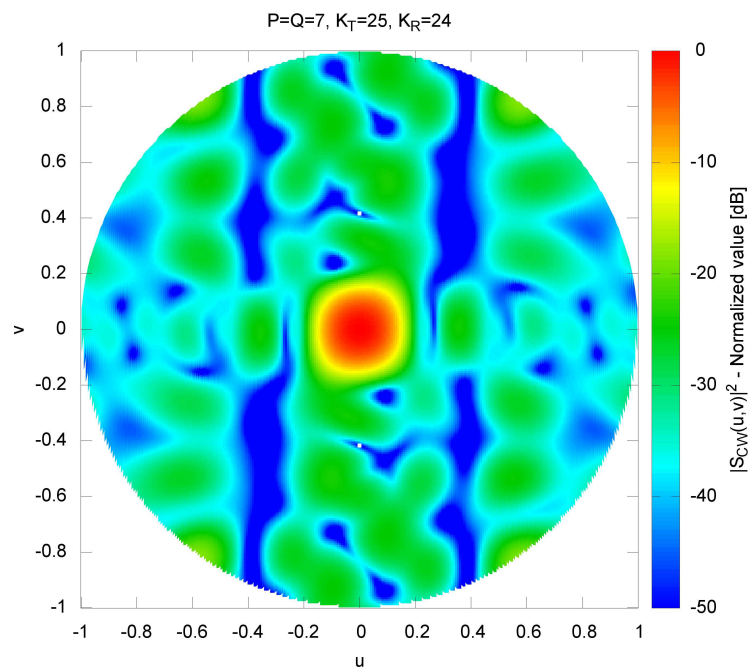


Figure 5 - G. Oliveri et al., “ADS-based Array Design for 2D and 3D Ultrasound Imaging”

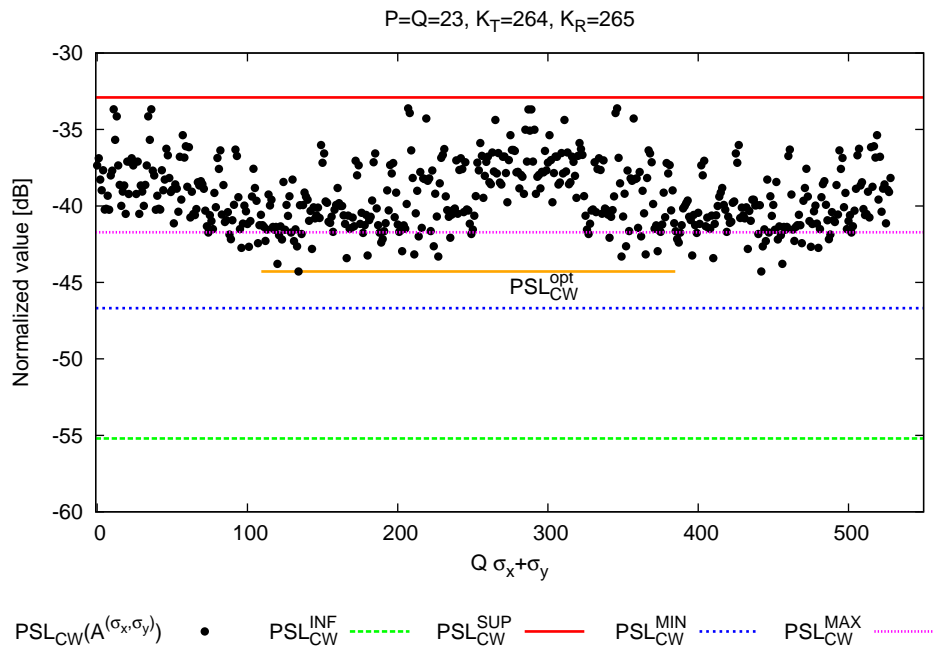


(a)

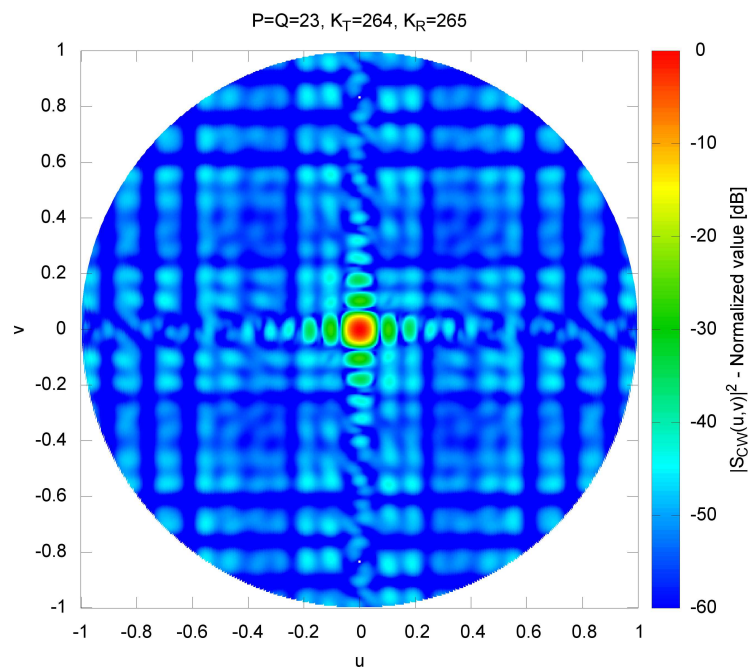


(b)

Figure 6 - G. Oliveri et al., “ADS-based Array Design for 2D and 3D Ultrasound Imaging”

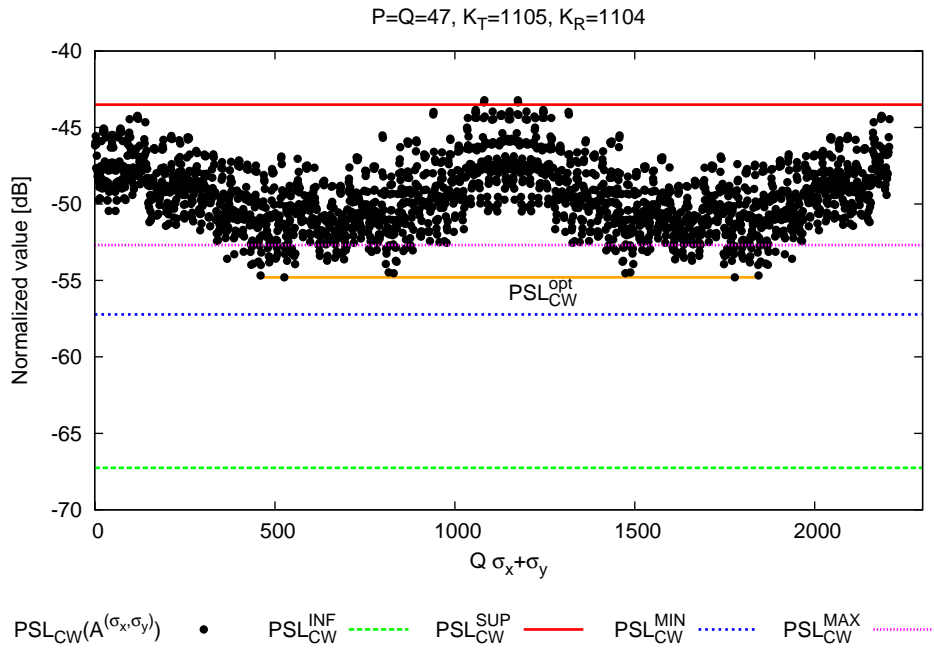


(a)

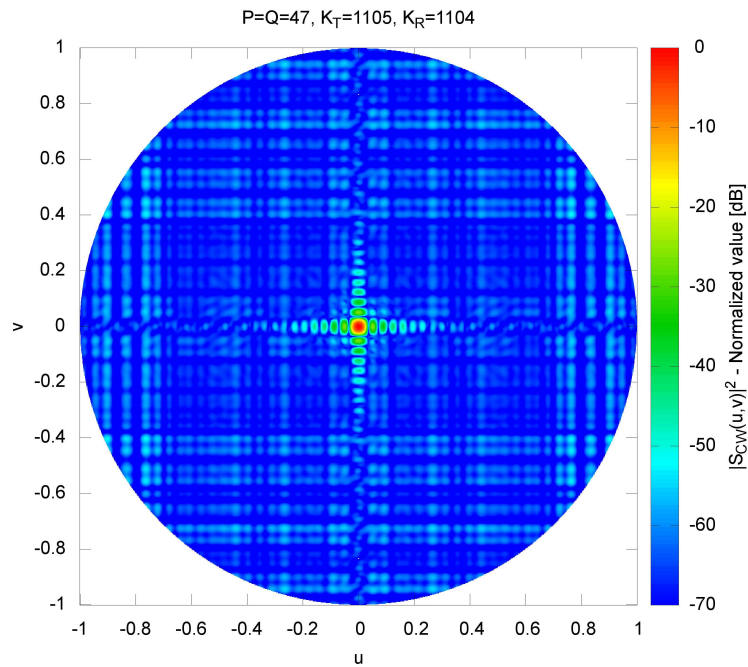


(b)

Figure 7 - G. Oliveri et al., “ADS-based Array Design for 2D and 3D Ultrasound Imaging”



(a)



(b)

Figure 8 - G. Oliveri et al., “ADS-based Array Design for 2D and 3D Ultrasound Imaging”

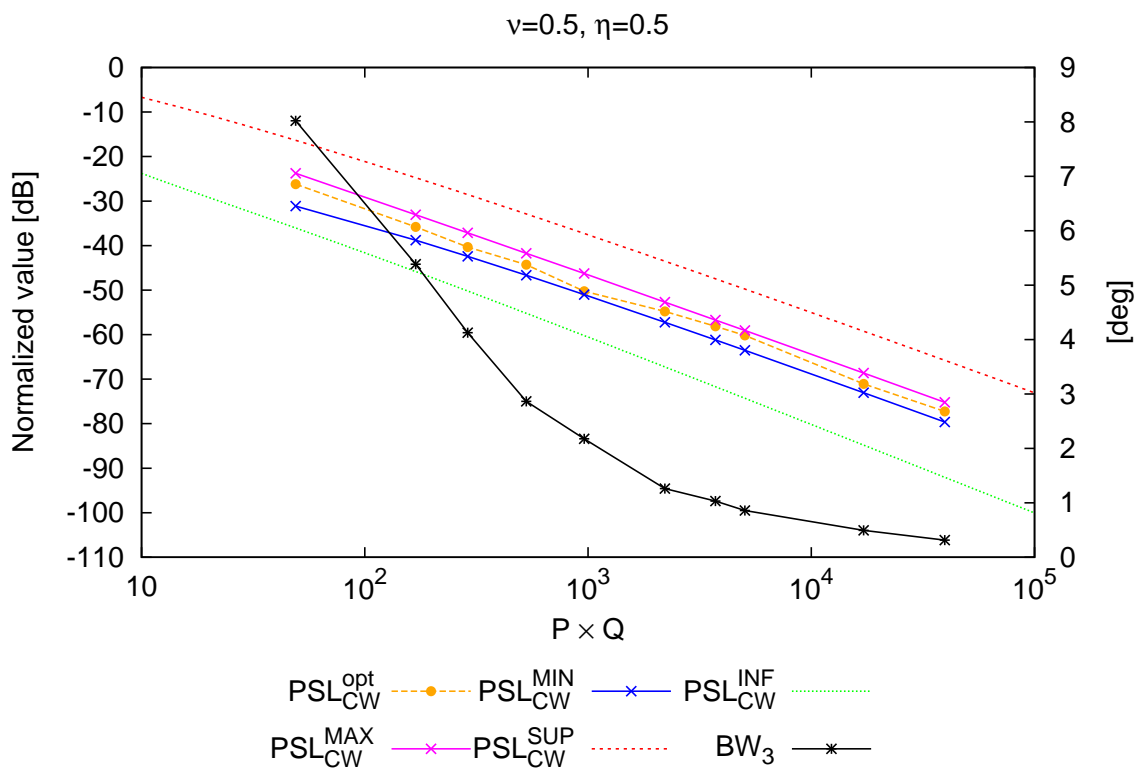
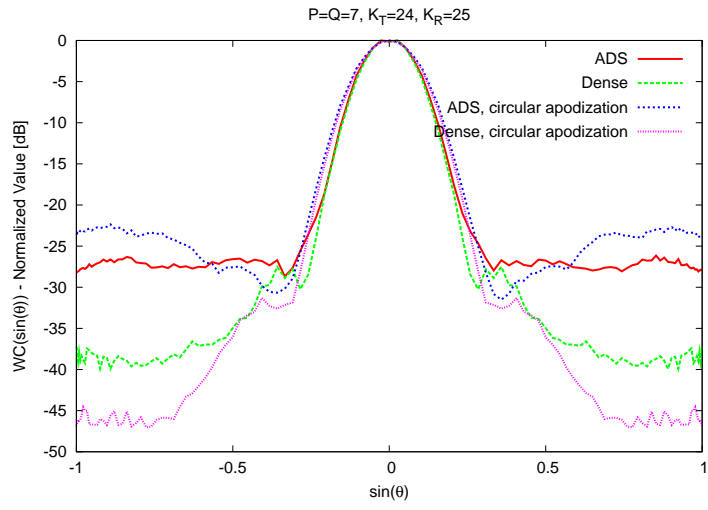
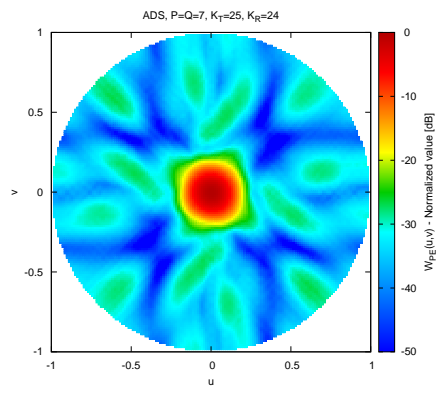


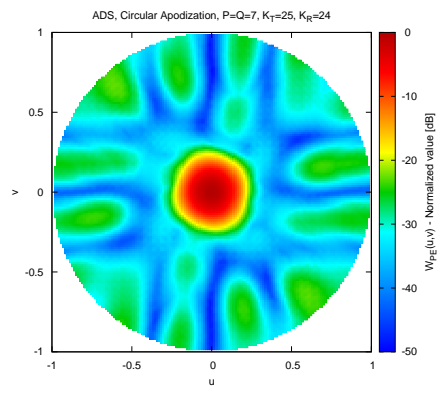
Figure 9 - G. Oliveri et al., “ADS-based Array Design for 2D and 3D Ultrasound Imaging”



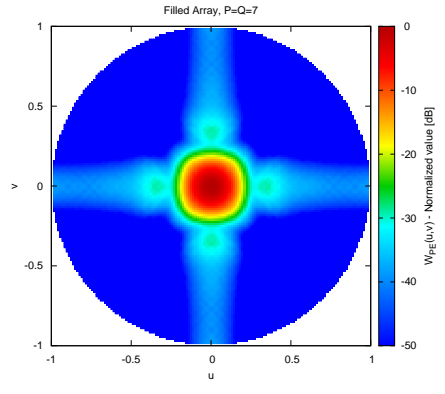
(a)



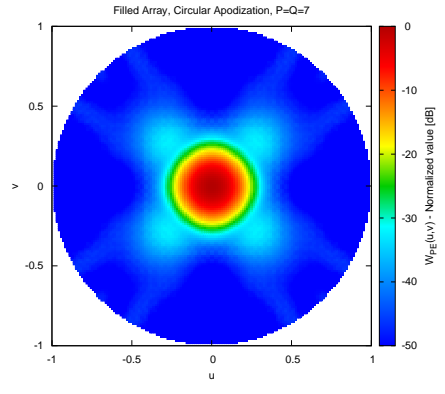
(b)



(c)

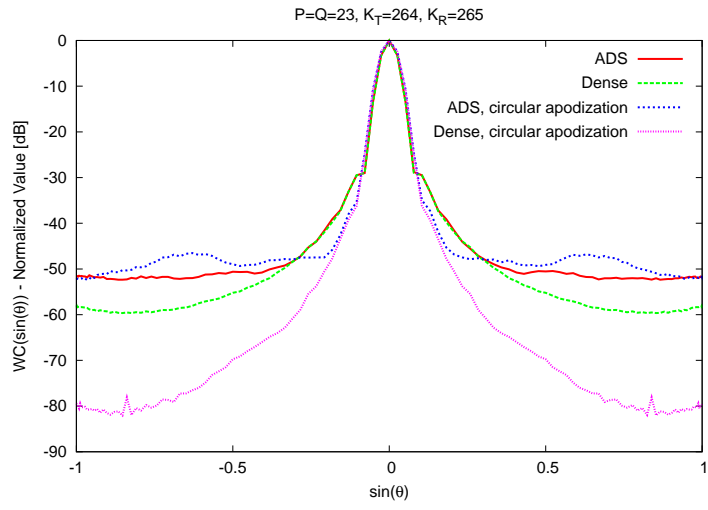


(d)

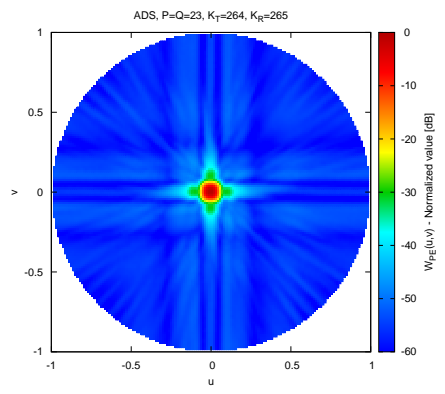


(e)

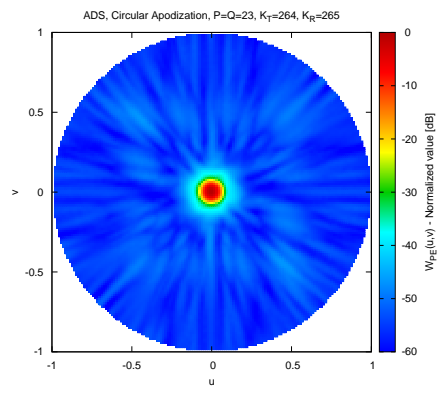
Figure 10 - G. Oliveri et al., “ADS-based Array Design for 2D and 3D Ultrasound Imaging”



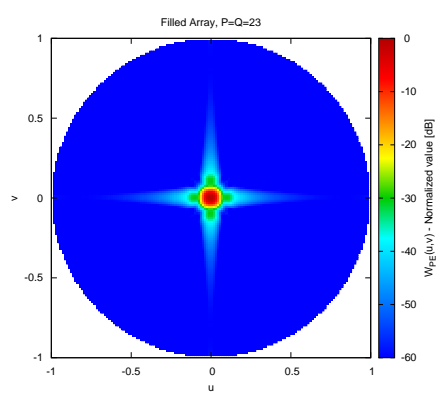
(a)



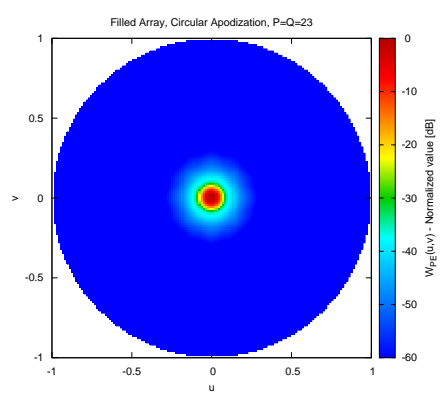
(b)



(c)

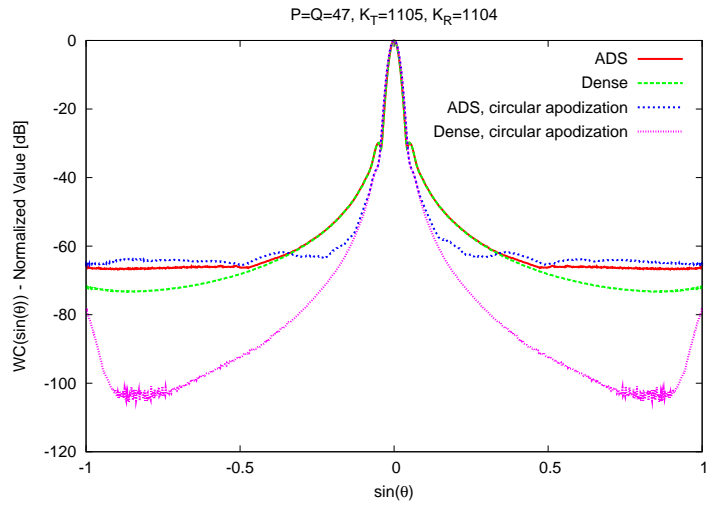


(d)

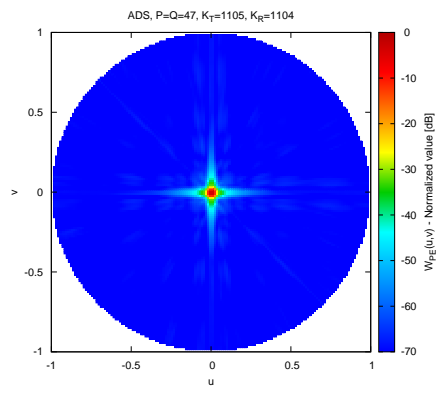


(e)

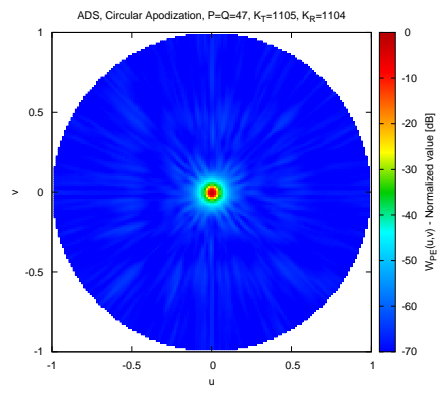
Figure 11 - G. Oliveri et al., “ADS-based Array Design for 2D and 3D Ultrasound Imaging”



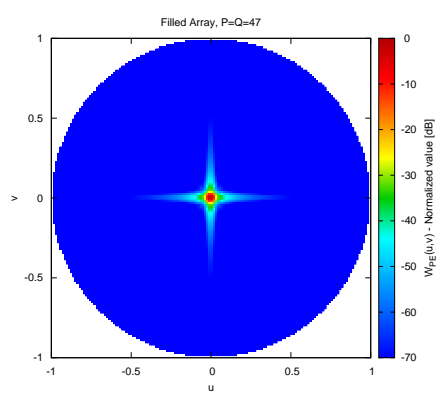
(a)



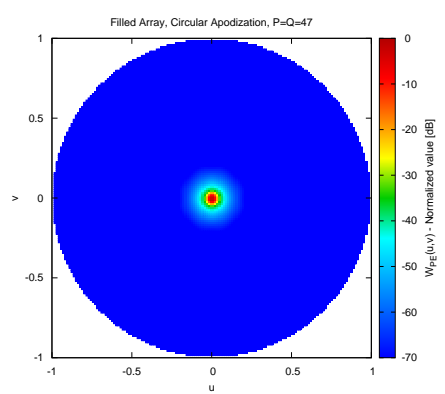
(b)



(c)

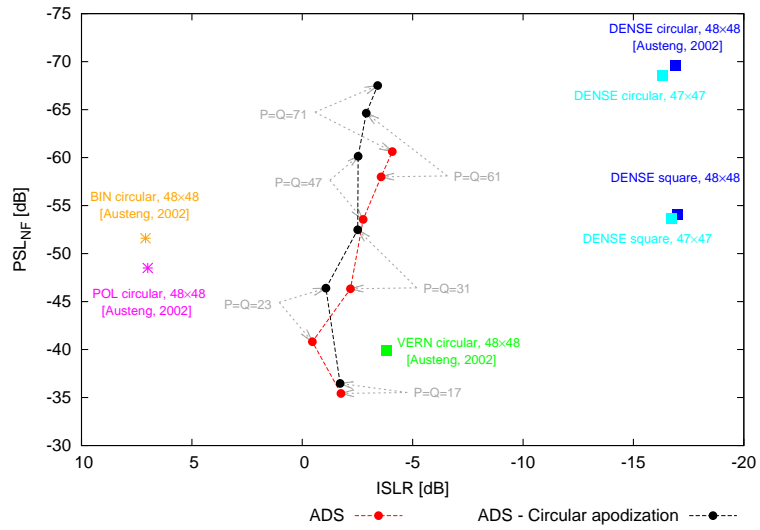


(d)

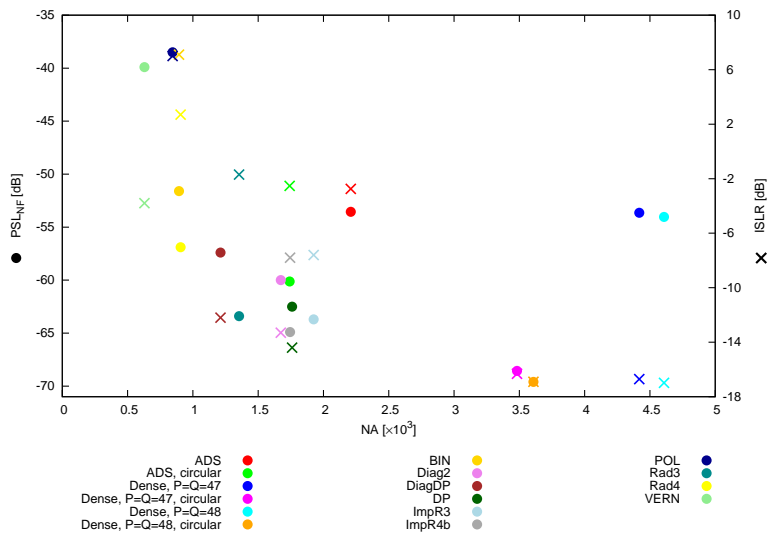


(e)

Figure 12 - G. Oliveri et al., “ADS-based Array Design for 2D and 3D Ultrasound Imaging”



(a)



(b)

Figure 13 - G. Oliveri et al., "ADS-based Array Design for 2D and 3D Ultrasound Imaging"

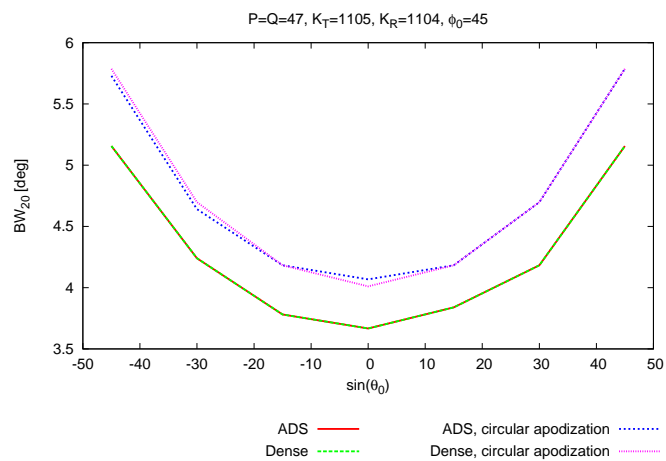
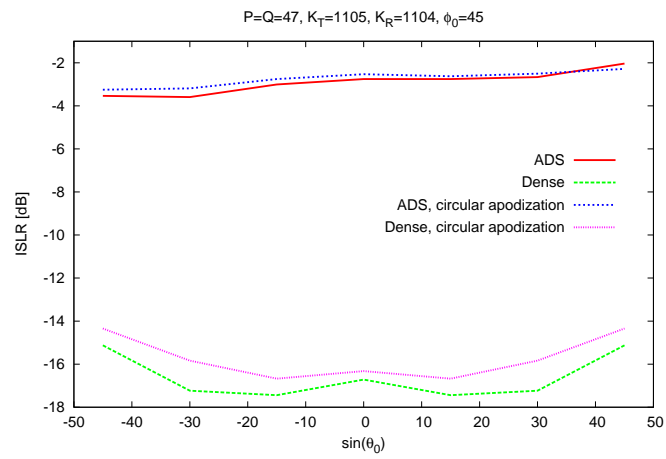
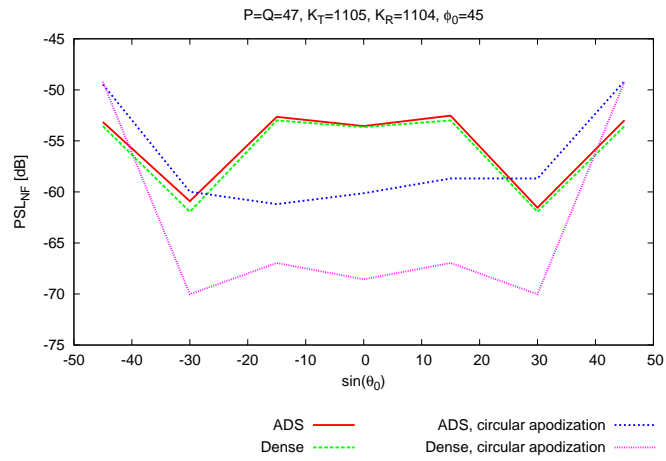
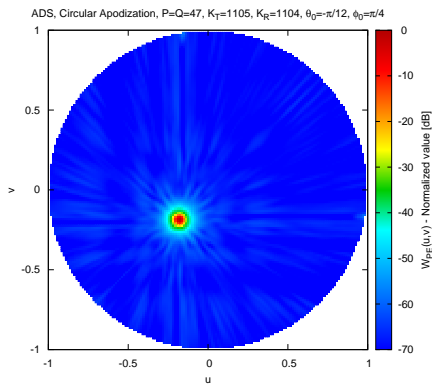
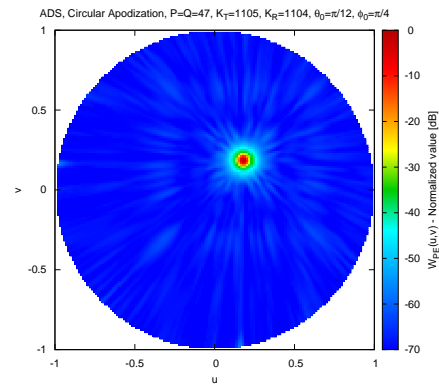


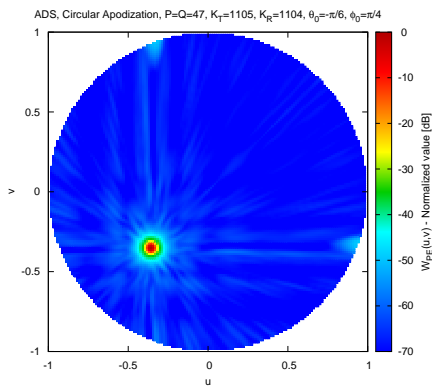
Figure 14 - G. Oliveri et al., “ADS-based Array Design for 2D and 3D Ultrasound Imaging”



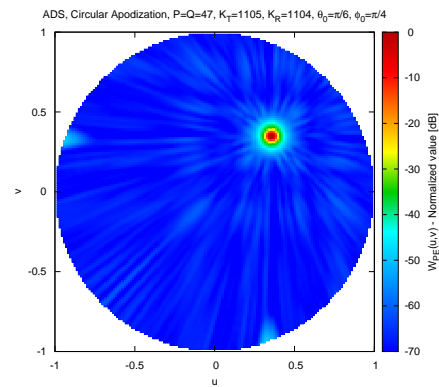
(a)



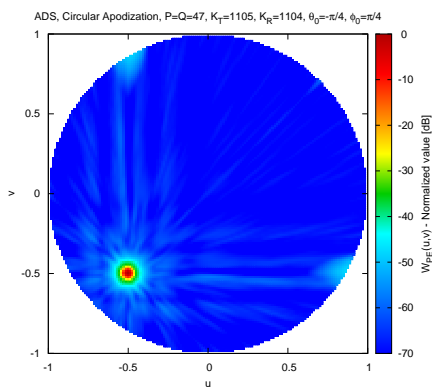
(b)



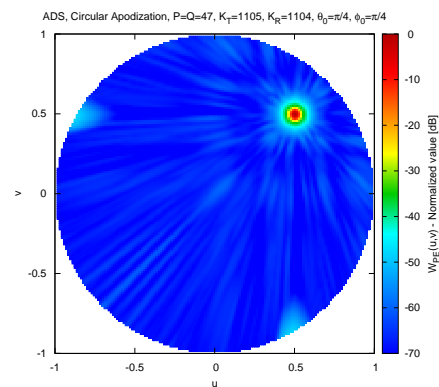
(c)



(d)



(e)



(f)

Figure 15 - G. Oliveri et al., “ADS-based Array Design for 2D and 3D Ultrasound Imaging”

Table I - G. Oliveri et al., "ADS-based Array Design for 2D and 3D Ultrasound Imaging"

<i>Geometry</i>	PSL_{CW}^{INF}	PSL_{CW}^{MIN}	PSL_{CW}^{MAX}	PSL_{CW}^{SUP}
Linear	$\left[\frac{K_T - \Lambda_T - 1 - \sqrt{\frac{t(N-t)}{N-1}}}{K_T(N-K_T)} \right]^2$	$\frac{\Xi_T^{max} \Xi_R^{max}}{K_T^2(N-K_T)^2}$	$\frac{[0.8488 + 1.128 \log_{10} N]^2 \Xi_T^{max} \Xi_R^{max}}{K_T^2(N-K_T)^2}$	$\frac{\{[0.8488 + 1.128 \log_{10} N][K_T - \Lambda_T - 1 + \sqrt{t(N-t)}]\}^2}{[K_T^2(N-K_T)^2]}$
Planar	$\left[\frac{K_T - \Lambda_T - \sqrt{\frac{(t+1)(N-1-t)}{N-1}}}{K_T(N-K_T)} \right]^2$	$\frac{\Xi_T^{min} \Xi_R^{min} [0.5 + 0.8 \log_{10} N]^2}{K_T^2(N-K_T)^2}$	$\frac{[-0.1 + 1.5 \log_{10} N]^2 \Xi_T^{max} \Xi_R^{max}}{K_T^2(N-K_T)^2}$	$\frac{\{[-0.1 + 1.5 \log_{10} N][K_T - \Lambda_T + \sqrt{(t+1)(N-1-t)}]\}^2}{[K_T^2(N-K_T)^2]}$

Table II - G. Oliveri et al., "ADS-based Array Design for 2D and 3D Ultrasound Imaging"

Design	$P = Q$	NC	NT	NR	BW_6 [deg]	BW_{20} [deg]	BW_{50} [deg]	$ISLR$ [dB]	PSL_{NF} [dB]
Dense, square	7	49	49	49	13.52	24.86	(*)	-22.5	-17.5
Dense, circular	7	37	37	37	15.12	27.67	(*)	-19.2	-14.1
(49, 25, 12, 24)-ADS	7	0	25	24	13.98	25.95	(*)	-28.9	-16.5
(49, 25, 12, 24)-ADS, circular	7	0	19	18	15.64	28.87	(*)	-36.1	-13.2
Dense, square	23	529	529	529	4.18	7.90	39.7	-17.3	-41.3
Dense, circular	23	421	421	421	4.69	8.47	23.49	-16.8	-49.7
(529, 265, 132, 264)-ADS	23	0	265	264	4.23	7.96	108.69	-0.4	-40.8
(529, 265, 132, 264)-ADS - circular	23	0	211	210	4.69	8.47	44.5	-1.1	-46.4
Dense, square	47	2209	2209	2209	2.00	3.66	18.67	-16.7	-53.6
Dense, circular	47	1741	1741	1741	2.29	4.01	11.17	-16.3	-68.6
(2209, 1105, 552, 1104)-ADS	47	0	1105	1104	2.00	3.66	18.67	-2.8	-53.6
(2209, 1105, 552, 1104)-ADS, circular	47	0	871	870	2.29	4.06	12.03	-2.5	-60.1

(*) Computation not feasible since $WC(\sin(\theta))$ doesn't reach -50 dB.

Table III - G. Oliveri et al., "ADS-based Array Design for 2D and 3D Ultrasound Imaging"

Design	$P = Q$	NC	NT	NR	BW_6 [deg]	BW_{20} [deg]	BW_{50} [deg]	$ISLR$ [dB]	PSL_{NF} [dB]
Dense, square	48	2304	2304	2304	1.83	4.52	18.27	-17.0	-54.0
Dense, circular [1]	48	1804	1804	1804	2.03	3.81	10.82	-16.9	-69.6
VERN [1]	48	48	421	208	2.05	3.83	10.65	-3.8	-39.9
BIN [1]	48	0	447	447	2.05	3.84	11.34	7.1	-51.6
POL [1]	48	0	484	361	2.25	4.15	8.10	7.0	-48.5
Diag2 [1]	48	396	877	296	2.05	3.84	11.09	-13.3	-60.0
DP [1]	48	428	880	880	2.05	3.85	11.21	-14.4	-62.5
DiagDP [1]	48	208	606	606	2.02	3.79	10.65	-12.2	-57.4
Rad4 [1]	48	69	533	373	2.21	4.11	12.66	2.7	-56.9
Rad3 [1]	48	221	821	533	2.13	4.00	11.63	-1.7	-63.4
ImpR3 [1]	48	551	821	1104	2.12	3.97	11.72	-7.6	-63.7
ImpR4b [1]	48	484	964	780	2.23	4.14	12.17	-7.8	-64.9